Journal of Hydrology 611 (2022) 128010

Contents lists available at ScienceDirect

Journal of Hydrology

journal homepage: www.elsevier.com/locate/jhydrol

Research papers

A distributed domain model coupling open channel flow and groundwater flow to quantify the impact of lateral hydrologic exchange on hydrograph

Song Wei [a,b], Yi Zheng [b,c,*], Xiuyu Liang [b,c], Peng Xu [b,c], Yong Tian [b,c], Jonathan M. Frame [d], Yong Zhang [d,*]

[a] Guangxi Key Laboratory of Environmental Pollution Control Theory and Technology, Guilin University of Technology, Guilin 541004, China
[b] School of Environmental Science and Engineering, Southern University of Science and Technology, Shenzhen 518055, Guangdong Province, China
[c] Shenzhen Municipal Engineering Lab of Environmental IoT Technologies, Southern University of Science and Technology, Shenzhen 518055, Guangdong Province, China
[d] Department of Geological Sciences, University of Alabama, Tuscaloosa, AL 35487, USA

ARTICLE INFO

This manuscript was handled by Huaming Guo, Editor-in-Chief

Keywords:
Lateral HEFs
Distributed-domain coupling model
Spatial heterogeneity
Power-law decay
Multi-rate flow

ABSTRACT

Hydrologic exchange flows (HEFs) of river-aquifer systems are known to affect water flow, but the quantitative influences of lateral HEFs and the riparian zone's hydraulic conductivity (*K*) distribution on stream fluxes remain obscure under varying hydrologic conditions. To fill this knowledge gap, this study proposed a physical based, distributed domain, coupled (open channel and groundwater) flow model (DDCM) to quantify the effect of lateral HEFs on hydrograph characteristics, including especially the peak discharge and tailing decay which are practically important. Numerical experiments showed that (1) the interaction between the lateral HEFs and river hydrodynamics reduced the peak discharge and flood flow rates, (2) a heterogeneous *K* field of the riparian zone generated multi-rate HEFs (which then changed flow response) represented by the hydrographs with various declining rates (varying from exponential to power-law), significantly expanding the flow process, and (3) the probability density function of *K* also affected the tailing and peak of the hydrograph. A preliminary test showed that the DDCM captured the overall pattern of hydrographs observed from a catchment in the Wadi Ahin West, Oman. This study, therefore, provided a model-based quantification of the mechanisms and factors of the lateral HEFs affecting the hydrograph pattern in flood events, and further applications are needed to test the applicability of the DDCM in capturing real-world hydrographs affected by the lateral HEFs.

1. Introduction

Hydrologic exchange flows (HEFs) affect solute transport in river-riparian systems, especially when the river stage fluctuates, which in turn affects aquatic ecosystems and biogeochemical cycles (Brunke and Gonser, 1997; Krause et al., 2011; Ward et al., 2013; Boano et al., 2014; Kiel and Cardenas, 2014; Zimmer and Lautz, 2014; Bernard-Jannin et al., 2016; Trauth and Fleckenstein, 2017; Liang et al., 2018). HEFs involve bidirectional fluxes vertically and/or laterally, typically in hyporheic zones, riverbanks, and floodplains (Jung et al., 2004; Cardenas, 2009a; Cardenas, 2009b; Harvey and Gooseff, 2015; Allgeier et al., 2021). Vertical HEFs mainly refer to the interaction between river water and water in riverbed sediments, while lateral HEFs refer to the interaction between river water and groundwater in bank sediments (Cardenas, 2009a; Cardenas, 2009b; Kiel and Cardenas, 2014). HEFs can prolong the contact time between river water and alluvium and further alter the residence time distribution of water traveling through the catchment, eventually affecting water quality and quantity (Jones and Mulholland, 1999; Kirchner et al., 2000; Cardenas, 2008). HEFs occurring between a river channel and riverbank can significantly affect hydrographs, if the discharge condition changes especially under overbank flooding (Hunt, 1990; Doble et al., 2012; Francis et al., 2015; Liang et al., 2020). HEFs may also lead to a delayed streamflow response and solute retention (Haggerty et al., 2002; Cardenas et al., 2004; Kirchner and Colin, 2013; Gomez-Velez et al., 2017). The mechanisms of HEFs affecting the peak and tailing behavior of hydrographs, however, have not been sufficiently explored, especially under flood event conditions (Dudley-Southern and Binley, 2015; Liang et al., 2018). This knowledge gap motivated this study.

HEFs are mainly influenced by the spatiotemporal variation of the

* Corresponding authors.
E-mail addresses: zhengy@sustech.edu.cn (Y. Zheng), yzhang264@ua.edu (Y. Zhang).

https://doi.org/10.1016/j.jhydrol.2022.128010
Received 29 December 2021; Received in revised form 25 May 2022; Accepted 27 May 2022
Available online 2 June 2022

hydraulic gradient and the distribution of hydraulic conductivity (*K*) within the river-aquifer system (Cardenas et al., 2004; Harvey and Gooseff, 2015; Liu et al., 2020; Shuai et al., 2019; Storey et al., 2003). With a constant river discharge, the hydraulic gradient is in steady state controlled by channel morphology, including individual stream reaches (Wondzell, 2006), channel sinuosity (Boano et al., 2006) and bedform (Wörman et al., 2002). With a changing river discharge, the hydraulic gradient is mainly affected by river stage fluctuations. A river stage higher than the riparian zone hydraulic head causes water to infiltrate into the riparian zone, while a lower river stage leads to a return flow from the riparian zone to the river channel (Cardenas et al., 2004; Liang et al., 2018) (Fig. 1).

The *K* distribution of the riparian zone, which is mainly affected by the spatial heterogeneity of soil physical properties (Jiang et al., 2015; Zeleke and Si, 2005; Zhang et al., 2014), also influences the magnitude and paths of HEFs. Currently, many field studies focus on the impact of the system's heterogeneity on hyporheic exchange at the reach scale, while few field experiments have been performed at the watershed scale. For example, Anibas et al. (2011) developed a thermal mapping method to study the surface water-groundwater interaction in one section of the Aa River, Belgium, and found that the *K* of riverbed sediment is a crucial factor that affects hyporheic exchange. Wang et al. (2017) applied Darcian flux calculations and the vertical streambed temperature profile approach to study the spatial variability in streambed vertical *K* for three types of streambed morphologies. They investigated the correlation between water flux, *K*, and hydraulic head at three sites in the Beiluo River, China. In addition, Cardenas (2008) found that the spatial heterogeneity of the riparian-hyporheic zone was associated with the late-time tailing behavior of water flow and solute transport.

Field experiments and numerical models provide common and reliable approaches to investigate the HEF process under different flow conditions (Tonina and Buffington, 2007; Cardenas, 2009a; Cardenas, 2009b). Some studies applied trace tests (using chemicals and/or temperature) and the water balance approach to quantify HEFs along rivers (Wondzell, 2006; Payn et al., 2009; Westhoff et al., 2011; Ward et al., 2013). Although field experiments provide direct data to analyze HEFs, these experiments, if applied alone, mainly produce case-specific results, rather than general implications. Reliable and testable numerical models can provide insights into hydrodynamic processes. Many modeling studies have been conducted to interpret the interaction between HEFs and hydrographs (Åkesson et al., 2015). For example, Pinder and Sauer (1971) proposed a coupled model to simulate the river-aquifer interaction, which contains a one-dimensional (1-D) open channel flow equation and a 2-D transient groundwater flow equation. Their numerical results showed that the hydrologic exchange process attenuated the flood peak and could lead to a late-time tailing behavior of the stream hydrograph. Harvey and Bencala (1993) used a 2-D hydraulic model to investigate the influence of streambed topography on HEFs and found that both the variation in stream water slope and the stepped-bed morphology controlled the water and solute exchange between the stream and subsurface water. Schmadel et al. (2016) developed a comprehensive model to simulate the hyporheic flux between the streams and hillslope under diel hydrologic fluctuation conditions and found that dynamic boundary conditions could extend the hyporheic flow path. Gomez-Velez et al. (2017) employed both the 2-D Boussinesq equation and the advection–dispersion equation to investigate hot spots and moments within the hyporheic zone, including the influence of channel sinuosity and *K* on hydrologic exchange. They found that the inflow and outflow of the hyporheic zone showed power-law tailing behaviors. Liang et al. (2018) proposed an analytical model based on the Boussinesq equation and studied the spatiotemporal variations in inflow and return flow under flooding conditions, and their model demonstrated that the return flow exhibited power-law attenuation after a flood event. Most of the studies reviewed above used the river stage (or discharge) as a known boundary condition to study the influence of the hydrodynamic process on HEFs without considering the influence of HEFs on the streamflow response. In addition, only a few modeling studies had investigated the influence of the watershed spatial heterogeneity on the hydrograph tailing behavior, although this issue had been frequently mentioned and well documented in field studies (Kirchner et al., 2000; Cardenas, 2008; Kollet and Maxwell, 2008).

In the literature reviewed right above, it was often found that the hydrographs observed in the field presented tailing behavior, but few studies used mathematical models for quantitative analysis. In this current study, a physical based, distributed domain, coupled (open channel flow and groundwater flow) model (DDCM) was proposed to quantitatively investigate the impact of the lateral HEF process on the pattern of hydrographs under dynamic flow conditions. The coupled

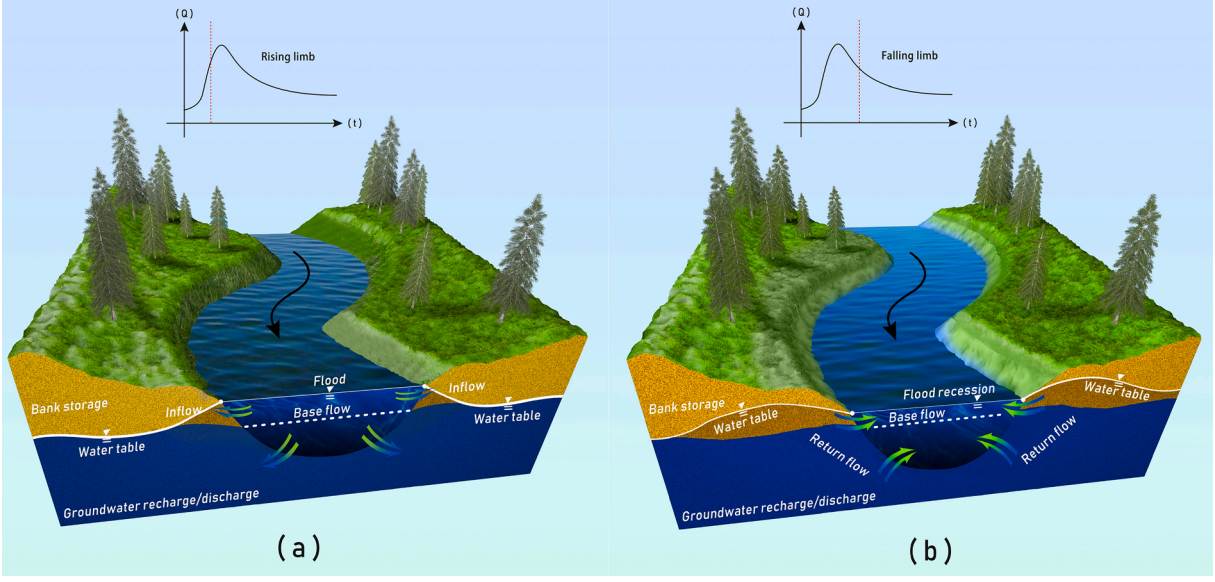

Fig. 1. Conceptual diagram of the interaction between the river channel and riparian zone under flood conditions quantified by this study. (a) During the flood arrival period, and (b) during the flood recession period. When the flood arrives, the river water begins to flow into the hyporheic zone and bank storage (inflow), and the water table rises, as shown in (a). After the flood peak passes, the river stage decreases rapidly. When the river level is below the riparian water table, the subsurface water recharges the river (return flow), as shown in (b).

processes of hydrologic exchange and river hydrodynamics were studied through a series of numerical experiments. This study aimed to address the following key questions: (1) How do river channel characteristics affect these coupled processes under flood event conditions? (2) How does the spatial distribution of hydraulic conductivity affect the hydrograph? (3) What factors will lead to a power-law tailing behavior of a streamflow?

The remainder of this work is organized as follows. Sections 2 and 3 show the development of the new model and the synthetic scenarios, respectively. Sections 4 and 5 discuss the numerical results and the preliminary application, respectively. Section 6 draws the final conclusions.

2. Model development and distribution function

Our model (DDCM) couples the open channel flow with the riparian groundwater dynamics. A rectangular domain is considered which includes a river channel and aquifers on both sides of the river (Fig. 2). The river flow direction is along the y-axis, the length and width of the river channel are L and B_r, respectively, and the distance between the lateral groundwater boundary and the river channel is denoted as b. The aquifers are assumed to be heterogeneous and isotropic. The aquifer on each side is underlain by an aquitard and is connected to the river channel.

The river flow is described by the 1-D Saint Venant equation, and the groundwater flow is described by the 2-D nonlinear Boussinesq equation. The dynamic hydrologic exchange between the river and groundwater follows Darcy's law:

$$q_{Gr} = Kh\frac{(H_G - Z_r)}{dx} \tag{1}$$

where q_{Gr} represents the lateral hydrologic exchange flux from the groundwater to the river flow per unit length [L^2T^{-1}], with subscripts "G" and "r" indicating groundwater and river flow, respectively (so q_{rG} represents the exchange flux from river to groundwater); K is the hydraulic conductivity [LT^{-1}]; h is the thickness of water flow in the aquifer (lateral hyporheic zone) [L]; H_G is the groundwater hydraulic head [L] and $H_G(x,y) = h(x,y) + (L-y)J$ where J is the water surface slope [-]; Z_r is the river stage [L]; and dx is the space step size in the x-direction. The coupled model consists of two parts shown below.

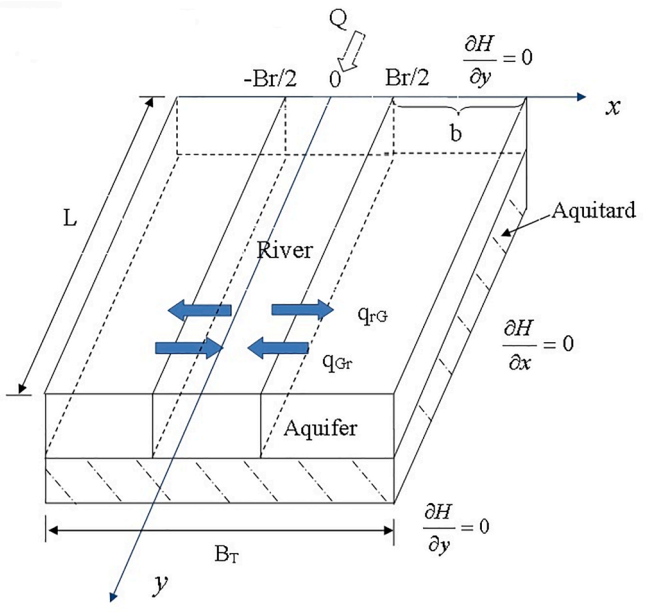

Fig. 2. Schematic diagram of the proposed river-aquifer system and the DDCM (coupling the 1-D Saint Venant equation and the 2-D Boussinesq equation). The blue arrows indicate the bidirectional water exchange between river and riparian zones. (For interpretation of the references to colour in this figure legend, the reader is referred to the web version of this article.)

(1) Open channel flow model

$$\frac{\partial A_r}{\partial t} + \frac{\partial Q_r}{\partial y} = q_L + q_{Gr} \tag{2a}$$

$$\frac{\partial Q_r}{\partial t} + 2u_r\frac{\partial Q_r}{\partial y} + \left(gA_r - B_r u_r^2\right)\frac{\partial Z_r}{\partial y} - u_r^2\frac{\partial A_r}{\partial y}\bigg|_{Z_r=const} + g\frac{Q_r|Q_r|}{A_r C^2 R} = 0 \tag{2b}$$

$$q_{Gr} = Kh(H_G - Z_r)/dx \tag{2c}$$

$$Q_r(y,0) = I_0(y); Z_r(y,0) = Z_0(y) \tag{2d}$$

$$Q_r(0,t) = f_1(t); Q_r(L,t) = f_2(Z_r(L,t)) \tag{2e}$$

where Q_r is the river discharge [L^3T^{-1}]; q_L is the source/sink term [L^2T^{-1}]; u_r is the river flow velocity [L^1T^{-1}]; g is the gravitational acceleration [LT^{-2}]; A_r is the cross-sectional area of the river [L^2]; C is the Chézy coefficient [$L^{1/2}T^{-1}$] which is equal to $\frac{1}{n_c}\sqrt[6]{R}$; n_c is the coefficient of roughness; R denotes the hydraulic radius [L]; I_0 [L^3T^{-1}] and Z_0 [L] are the initial river discharge and river stage, respectively; f_1 is the river discharge at upstream; and f_2 describes the relationship of Q_r and Z_r at downstream.

(2) Groundwater flow model

$$\frac{\partial}{\partial x}\left(Kh\frac{\partial H_G}{\partial x}\right) + \frac{\partial}{\partial y}\left(Kh\frac{\partial H_G}{\partial y}\right) + W = S_y\frac{\partial H_G}{\partial t} \tag{3a}$$

$$H_G(x,y,0) = H_0 \tag{3b}$$

$$\frac{\partial H_G}{\partial x}\bigg|_{x=\pm\left(\frac{B_r}{2}+b\right)} = 0; \frac{\partial H_G}{\partial y}\bigg|_{y=0,L} = 0 \tag{3c}$$

$$\left(Kh\frac{\partial H_G}{\partial x}\right)\bigg|_{x=\pm\frac{B_r}{2}} = -q_{Gr} \tag{3d}$$

where W is the infiltration recharge of aquifer per unit area [L^1T^{-1}], and S_y is the specific yield [-].

The Preissmann scheme is adopted to solve the Saint Venant equation (2), as it is proved to be accurate and stable in solving the Saint Venant equation (Lyn and Goodwin, 1987). The 2-D Boussinesq equation (3) is solved by the alternating direction implicit (ADI) method, which is unconditionally stable for 2-D problems (Xue and Xie, 2007; Lapidus and Pinder, 1999).

(3) Distribution function

In this study, the gamma and lognormal distributions are used to generate the hydraulic conductivity in the heterogeneous aquifers. The two-parameter gamma distribution for a continuous random variable x is defined by a shape parameter α and a scale parameter β:

$$f_g(x) = \frac{1}{\beta^\alpha\Gamma(\alpha)}x^{\alpha-1}e^{-x/\beta}, x \geq 0.$$

The expected value of x following the gamma distribution is $E(x) = \alpha\beta$, and the variance is $var(x) = \alpha\beta^2$.

The bivariate lognormal distribution for the random variable x can be defined as follows:

$$f_l(x) = \frac{1}{x\sqrt{2\pi\sigma^2}}exp\left[-\frac{1}{2}\left(\frac{ln(x)-\mu}{\sigma}\right)^2\right](x>0)$$

where $\ln(x) \sim N(\mu, \sigma^2)$ is normally distributed with a mean μ and a standard deviation σ.

3. Synthetic case and numerical experiments

In this section, synthetic cases were used to test the DDCM and investigate how river channel characteristics control the hydrograph pattern.

In the synthetic cases, the total length and width of the river-aquifer segment conceptualized in Fig. 2 are $L_T = 10\ km$ and $B_T = 140\ m$, respectively, the river width is $B_r = 40\ m$, the coefficient of roughness is $n_c = 0.02$, and the water surface slope is $J = 0.002$. The initial stage of the river equals the initial equivalent pressure head of groundwater: $Z_0 = H_{G0} = 3\ m$. The width of the aquifer is $b = 50\ m$, and the specific yield is $S_y = 0.1$. These parameters can represent those for a regional-scale river-aquifer system, which are also appropriate for the dimension of a numerical test site. The space steps are $\Delta x = 2m$ and $\Delta y = 50\ m$, leading to 200 segments of river channel and 10,000 blocks of aquifer (5000 on each side of the river). According to the Manning formula ($u_r = \frac{1}{n_c}R^{2/3}J^{1/2}$), the background discharge is $Q_0 = 508.5\ m^3/s$, and the discharges in the numerical results are background-subtracted. The hydrographs are calculated at the location of $y = 10\ km$ (i.e., the downstream boundary).

As shown above, hydraulic conductivity K of the aquifers in this study follows the lognormal and gamma distributions (in different numerical experiments), which are two widely used probability density functions (PDFs) for hydrologic properties (Yue et al., 2001). The distribution of K of the aquifers on both banks of the river is symmetrical (i.e., the K values are mirrored). We randomly assign K values which obey the lognormal or gamma distribution to some sub-domains ($n = 100$) in one side of the study domain, and then interpolate the distribution of K in this side of the study domain ($25 \times 200 = 5{,}000$) using the simple Kriging method.

Without specific instructions, we assume that the unit hydrograph of upstream discharge (representing the boundary condition at the upstream location) satisfies the following form (Tunas, 2019):

$$q(t) = \left\{ \left(\frac{t}{T_P}\right) exp\left(1 - \frac{t}{T_P}\right) \right\}^{C_3} \tag{4a}$$

$$Q(t) = Q_P \bullet q(t) \tag{4b}$$

where $q(t)$ [dimensionless] is the unit hydrograph, T_P [T] is the arrival time of the flood peak, C_3 is the coefficient of the hydrograph shape, $Q(t)$ [L^3T^{-1}] is the upstream discharge, and Q_P [L^3T^{-1}] is the peak value of flood.

We conducted numerical experiments on the synthetic case described above to investigate the following three scenarios with increasing medium heterogeneity (where the corresponding parameters are listed in Table 1):

Scenario 1 (with a homogeneous K field): In this scenario, we investigate the effects of river system characteristics (i.e., K, B_r, J, and n_c) on the hydrograph in a homogenous K field ($K = 0.0005\ m/s$, representing the typical K for sorted sand). The incoming flow at the upstream location ($x = 0$) is a continuous source and satisfies the unit hydrograph formula (4) with $T_P = 1800\ s$, $C_3 = 2$, and $Q_P = 1000\ m^3/s$.

Scenario 2 (with one set of heterogeneous K fields): In this scenario, the effects of heterogeneous K of the aquifer on the hydrograph are studied. The river channel is divided into 200 sub-domains, and the random hydraulic conductivities K_i ($i = 1, 2, \ldots, 5000$) are assumed to follow the gamma or lognormal distribution. We explore the tailing behavior and peak portion of the hydrograph, which both vary with the change in the relative standard deviation (RSD) of K. The mean value of K is set as $0.0005\ m/s$, and the RSD varies from 0 to 1.5. The initial and boundary conditions are the same as those used for **Scenario 1**.

Scenario 3 (with multiple sets of heterogeneous K fields): To identify the river system characteristics controlling the tailing behavior of the hydrograph, we generated 100 sets of random K_i for each case (which satisfies the lognormal or gamma distribution with the RSD equal to 0.5, 1.0, and 1.5, respectively) in simulating the hydrographs. Effects of the K_i distribution range and the variation of K on hydrograph patterns are analyzed. The mean value of K is $0.0005\ m/s$, and the initial and boundary conditions are the same as those used for **Scenario 1**.

4. Results and discussion

4.1. Impacts of river system characteristics on hydrograph

The main results from **Scenario 1** are presented in Fig. 3. As shown in Fig. 3a, when the lateral HEFs are not considered (i.e., $K = 0$), the peak discharge downstream ($x = 10\ km$) is $937.7\ m^3/s$, and the peak arrival time is $2960\ s$. If $K = 0.0005\ m/s$, the peak discharge downstream is $408.7\ m^3/s$ (56.4% deduction), and the peak arrival time is $3800\ s$ (28.4% delay). Fig. 3a also indicates that with an increasing K, the tail of hydrographs becomes heavier. Hence, the hydrologic exchange effect can reduce the flood peak discharge and slow down the arrival time of the flood peak. The reduced discharge in river is temporarily stored in the lateral hyporheic zone. Then it is slowly released if the river stage is lower than that of the hyporheic zone, causing the discharge tailing behavior.

Fig. 3b shows that the flow peak decreases with a decrease of B_r. The reason is that for a given inflow discharge upstream, the narrower the channel, the more the water level changes. This results in a greater hydrologic exchange rate and more river water entering the riparian zone. Therefore, for a wider river section, the contribution of lateral HEFs on flow discharge will be smaller. According to Manning's formula, it is expected that the flow peak decreases with the increasing n_c

Table 1
Statistics of the river-aquifer properties used in **Scenarios 1–3**. In the legend, "S" denotes "Scenario", "Hom" represents "Homogeneous", and "Het" represents "Heterogeneous".

Scenario	Figure	$\overline{K}(m/s)$	$B_r(m)$	J	n_c	Hom. or Het.
S1	Fig. 3a	Variable	40	0.002	0.02	Hom.
	Fig. 3b	0.0005	variable	0.002	0.02	Hom.
	Fig. 3c	0.0005	40	variable	0.02	Hom.
	Fig. 3d	0.0005	40	0.002	variable	Hom.
S2	Fig. 4a	0.0005	40	0.002	0.02	Het. (Gamma)
	Fig. 4b	0.0005	40	0.002	0.02	Het. (Lognormal)
S3	Fig. 5(a-c)	0.0005	40	0.002	0.02	Het. (Gamma)
	Fig. 5(d-f)	0.0005	40	0.002	0.02	Het. (Lognormal)
	Fig. 6a	Variable	40	0.002	0.02	Hom.
	Fig. 6b	Variable	40	0.002	0.02	Hom.
	Fig. 7a	0.0005	40	0.002	0.02	Het. (Gamma)
	Fig. 7b	0.0005	40	0.002	0.02	Het. (Lognormal)
	Fig. 7c	0.0005	40	0.002	0.02	Hom.
	Fig. 8a	0.0005	40	0.002	0.02	Het. (Gamma)
	Fig. 8b	0.0005	40	0.002	0.02	Het. (Lognormal)

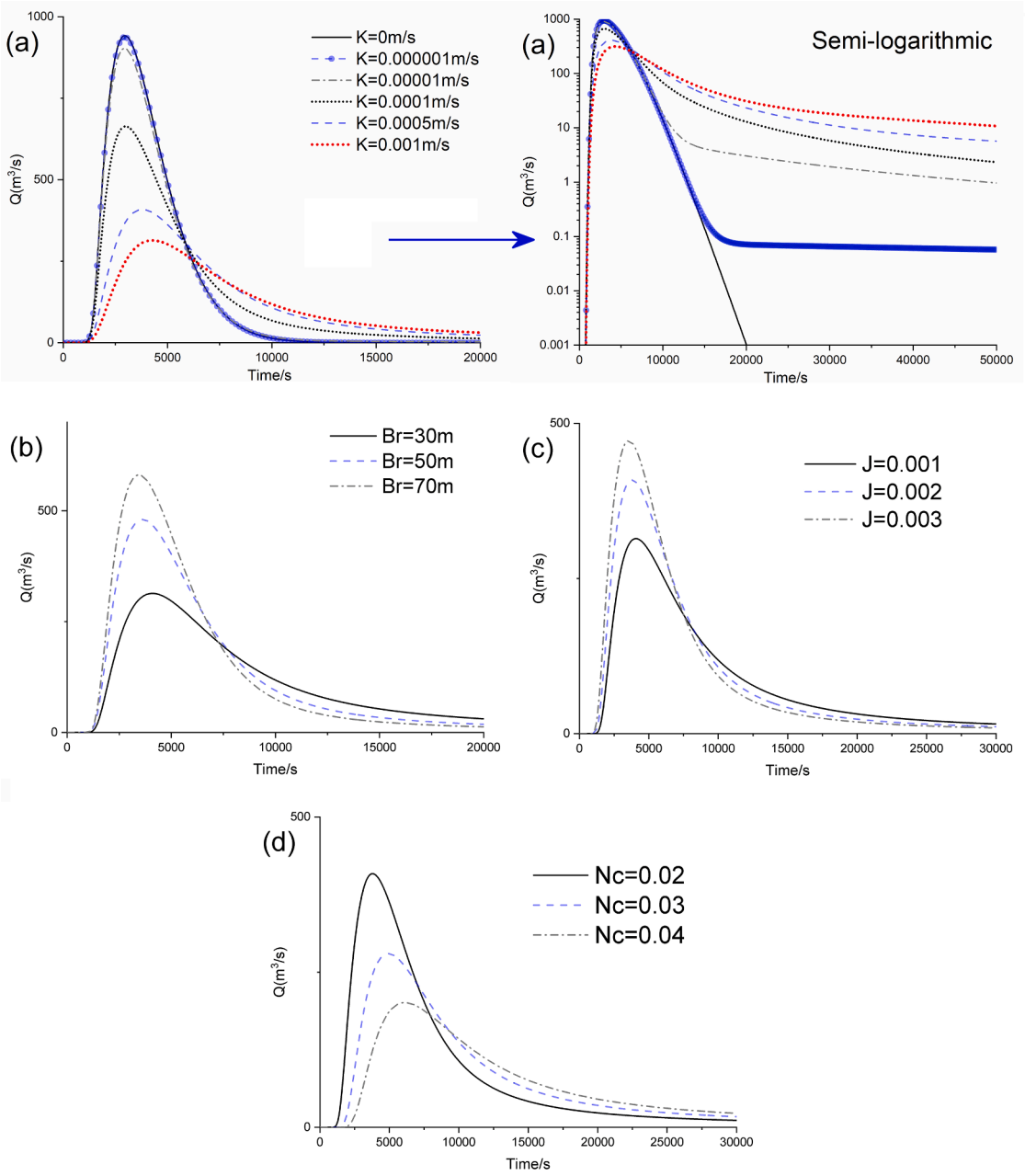

Fig. 3. Impact of river system characteristics (i.e., K, B_r, J, and n_c) on the hydrograph pattern. (a) shows the simulated hydrograph in different coordinate systems: the top left plot is in the Cartesian coordinate to show the effect of K on the flood peak, and the top right plot uses the semi-logarithmic coordinate to emphasize the hydrograph tailing behavior affected by K.

and increases with the increase in J. Meanwhile, as shown in Fig. 3c and 3d, the tailing behavior of hydrographs becomes heavier with the increase in n_c and the decrease in J. In addition to the fact that a reduction of J (or an increase of n_c) itself would lead to a decrease in flow velocity (flow discharge), it would also lead to an increasing exchange time between the river and the riparian zone, which would further reduce the peak value and enhance the hydrograph tailing.

According to the analysis shown above, due to the hydrologic exchange process, riverbanks can reduce the peak discharge. Thus, information on the permeability of the riparian zone within catchments can be important for flood control planning and flood forecasting. HEFs also change the river flow field and enhance the contact between contaminants and the alluvium, thus affecting the fate and transport of contaminants in the river-aquifer system.

4.2. Impacts of aquifer heterogeneity on hydrograph

Many real-world observations have shown that the flood hydrograph has tailing characteristics (Payn et al., 2009; Jencso et al., 2010; Baartman et al., 2012; Ward et al., 2013). These tailing behaviors vary from exponential decay to power-law decay with a broad variation range. Based on **Scenario 2**, the effect of hydrogeological heterogeneity on the hydrograph, particularly its tailing behavior, is investigated here by focusing on the commonly used gamma and lognormal distributions of K (Kirchner et al., 2000; Yue et al., 2001) listed in Section 2.

Fig. 4 shows that when the RSD of K increases, the long-term tail of the hydrograph gradually shifts from exponential decay to power-law decay. The reason may be that the random hydraulic conductivity of each sub-domain causes the HEFs to exhibit multi-rate characteristics. When the flood recedes, due to the contribution of multi-rate return

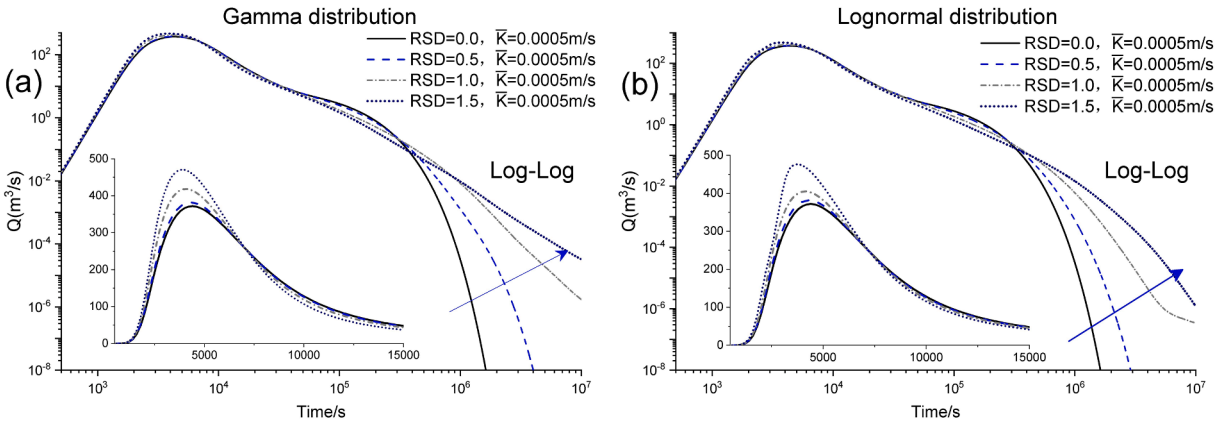

Fig. 4. Hydrographs affected by the RSD of K following the gamma distribution (a) or the lognormal distribution (b). The subfigure in each plot shows the hydrograph in a linear–linear coordinate, to emphasize the hydrograph peak.

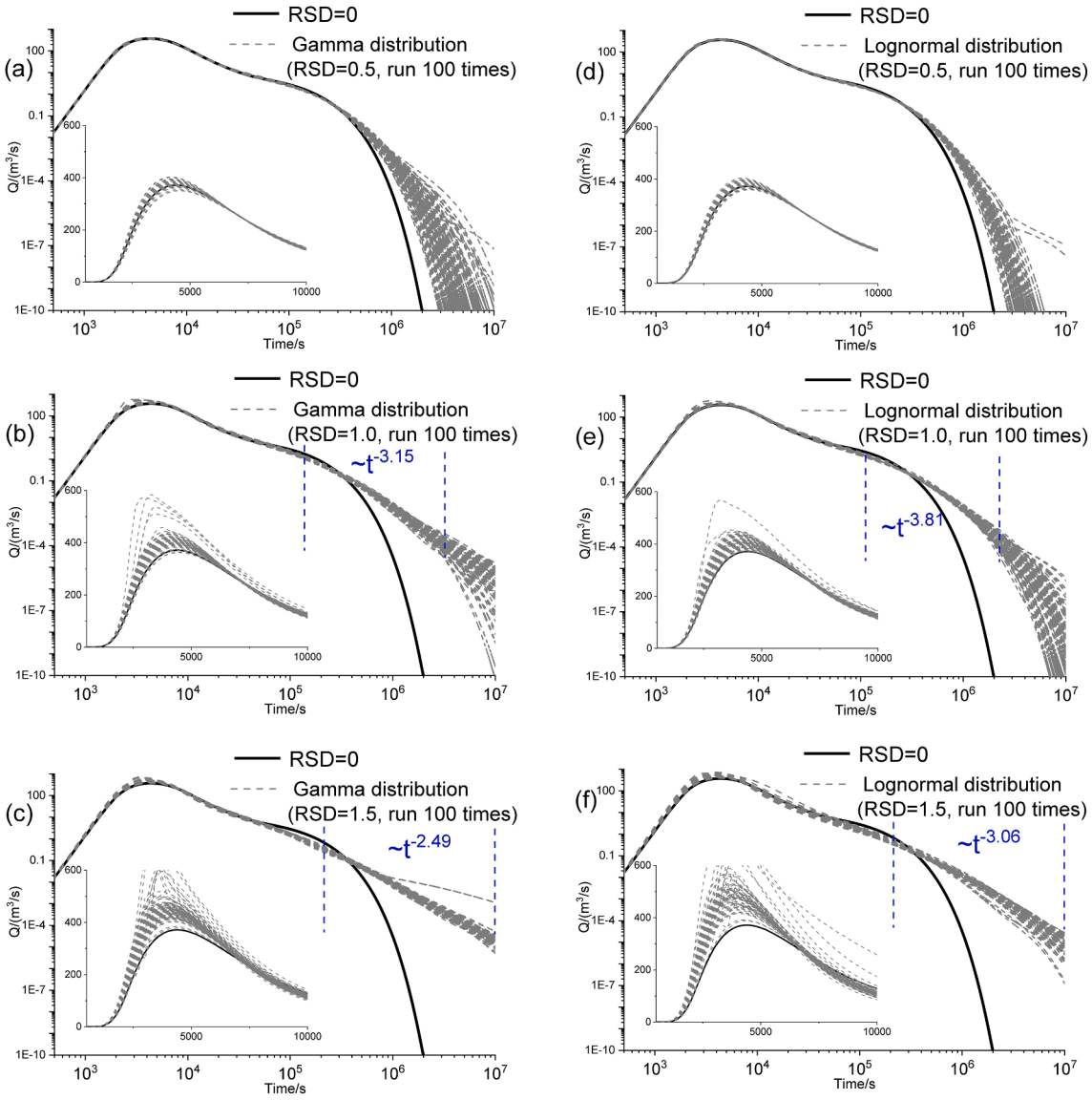

Fig. 5. Hydrographs for K satisfying the gamma (left plots) and lognormal (right plots) distributions: (a-c) the gamma distribution with the relative standard deviation for K: RSD = 0.5, 1.0, and 1.5, respectively. (d-f) the lognormal distribution with RSD = 0.5, 1.0, and 1.5, respectively.

flows, the hydrograph declines slowly in a power-law form. The numerical results also show that regardless of the PDF of K (i.e., gamma or lognormal PDF), the hydrograph tailing behavior tends to decay in a power-law form when the RSD of K gradually increases. In general, the heterogeneous K of natural soil may be distributed according to the gamma or lognormal distribution. Soil heterogeneity tends to act as a converter by transforming the exponential decay process into the power-law decay process. This may explain the power-law decay phenomenon often observed in hydrologic processes in natural media.

The distribution of K in the riparian zone affects both the magnitude and the kinematic wave velocity of the peak flow through a river reach. It is shown that when K obeys the gamma or lognormal distribution, the hydrograph peak tends to increase with the increase in the RSD of K. It is our expectation that the increase of RSD will make the distribution of K more uneven, which will reduce the flow connectivity of the riparian zone, resulting in the decrease of the entire river-riparian water exchange capacity.

4.3. Factors controlling the hydrograph tailing behavior

The results shown above lead to the following two questions. First, if K satisfies the gamma or lognormal distribution with a large RSD, does this scenario always lead to a power-law decay for the hydrograph tail? Second, why does the gamma distribution of K differ from the lognormal one in approaching the power-law tailing behavior in the hydrograph?

Scenario 3 addresses the two questions. For the first question, Fig. 5 shows that when the RSD of K increases from 0.5 to 1.5, the long-term tail of the hydrographs gradually changes from exponential decay to power-law decay, and the duration of the power-law decay increases. However, the power-law decay of the hydrograph does not persist, especially when K follows a lognormal distribution. As illustrated in Fig. 5, an increase of the RSD of K increases the average slope of the hydrograph's late-time tail. When K satisfies the gamma distribution, the hydrograph is more likely to exhibit a power-law decay tail with a longer duration than that with a lognormal distribution of K. Our explanation is the larger the RSD, the wider the distribution of the K, and it is more likely to have multi-rate return flows. These return flows have different discharge and arrival times when reaching downstream, which ultimately lead to the tailing behavior of the hydrograph.

To answer the second question, we first analyzed the influence of the change of K to the hydrograph. Fig. 6a shows that the smaller the K, the greater the influence of the change of K on the tailing behavior of the hydrograph. What is important is that K affects two aspects of hydrograph tailing behaviors: (1) the larger the K, the heavier the tail; and (2) the larger the K, the earlier the tail will appear and the shorter the duration. Therefore, a single K value is not sufficient to cause a power-law decay for the late-time hydrograph. Fig. 6b shows the sensitivity ($\partial Q/\partial K$) of the peak discharge to K. When the K is smaller, the flood peak value is more sensitive to the change of K. In general, the hydrograph pattern is increasingly insensitive to the variation of K.

The spatial distributions of HEFs (q_{Gr}) were then evaluated here for different K distributions. The hydrograph tailing behavior is mainly affected by the return flow ($q_{Gr} > 0$). Here we selected $t = 9000\ s$ as the sampling time, since the flood peak had passed through the downstream section and groundwater was recharging the river ($q_{Gr} > 0$) after this time. As shown in Fig. 7a ~ 7c, when K followed the gamma distribution (RSD = 1.5), the lognormal distribution (RSD = 1.5), and the uniform distribution (RSD = 0), the resultant range of q_{Gr} (m^2/s) was (8.4×10^{-14}, 3.5×10^{-4}), (2.1×10^{-14}, 5.4×10^{-4}), and (3.8×10^{-5}, 1.2×10^{-4}), respectively. Therefore, the return flow presented a more pronounced multi-rate distribution if K had a broader distribution. Fig. 7d shows the return flow rates (in the total of $L/dy = 200$ sections) in descending order. The gamma distribution of K produced more low-velocity return flow regions (200–169 = 31 sections) than that of the lognormal distribution (200–187 = 13 sections), which might be more likely to cause power-law decay of the hydrograph tail. Notably, this assumption cannot be reliably proved by Fig. 7, since this figure shows only one snapshot (i.e., at a specific moment) of the HEFs, and the HEF vectors (including the magnitude and direction) may also change spatiotemporally and thence complicates the hydrography tailing behavior.

Finally, we analyzed the distribution range of K generated by the gamma and lognormal distributions with different RSDs. Fig. 8 compares the range of K values generated by the gamma/lognormal distribution when RSD = 1.5 and $\overline{K} = 0.0005\ m/s$. Table 2 lists the distribution ranges of K with different RSDs. Fig. 8 shows that in the semi-logarithmic coordinate, the K generated by the gamma distribution has a wider (or less "uniform") distribution than the K generated by the lognormal distribution, especially in the small value range (see also Table 2). This may cause the hydrological exchange process to produce multi-rate return flow, ultimately leading to the power-law tailing behavior of the hydrograph when K of the heterogeneous aquifer follows the gamma distribution. Notably, the gamma distribution is the combination of the power-law distribution and the exponential distribution. Therefore, when the K of the aquifer satisfies the gamma distribution and the RSD is large, the hydrograph's late-time tail generated by multi-

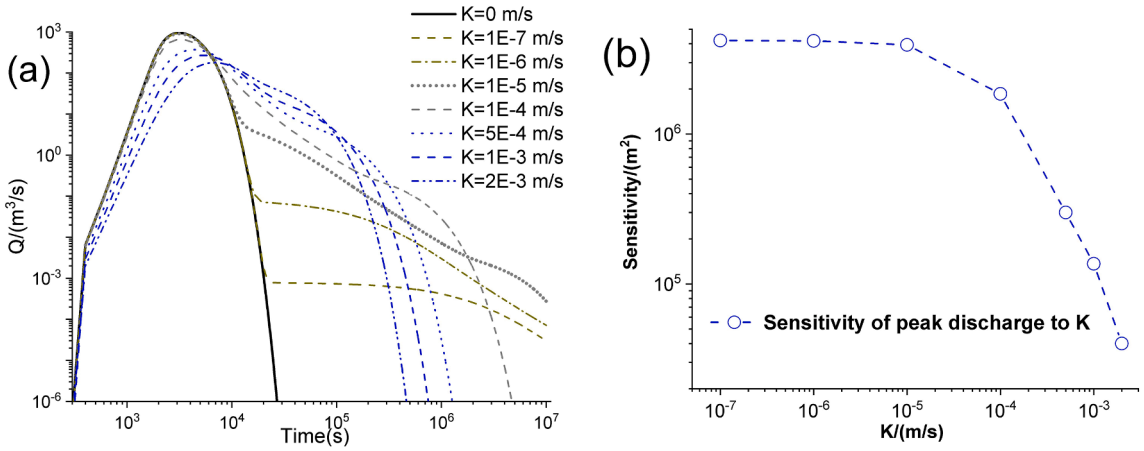

Fig. 6. The influence of the variation of K to the hydrograph pattern. (a) The influence of the change of K on the hydrograph tailing behavior. (b) The sensitivity (expressed by $\partial Q/\partial K$) of the peak discharge to K. A continuous inflow event is considered with the following parameters defined in Eq. (4): $T_P = 1800\ s$, $C_3 = 2$, and $Q_P = 1000\ m^3/s$, and the observation location is 10 km downstream.

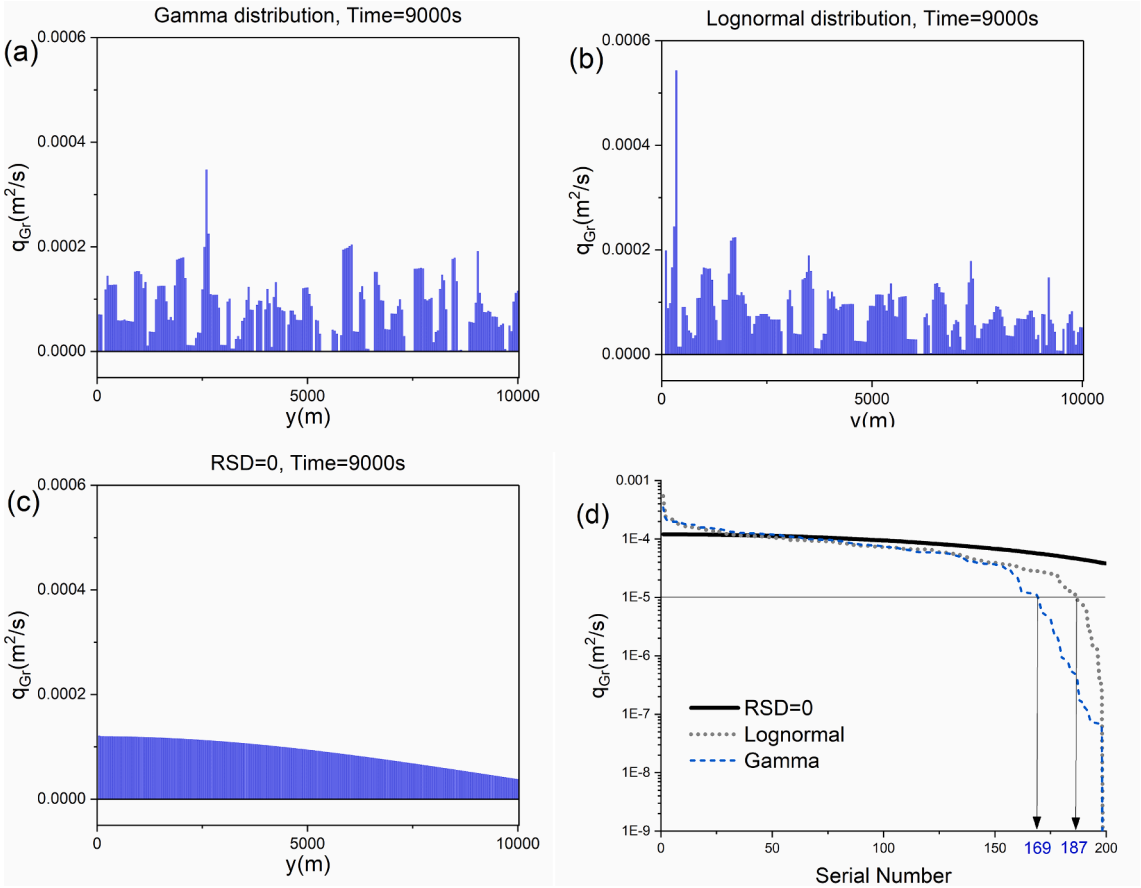

Fig. 7. The influence of the distribution of K on the HEFs (q_{Gr}) distribution along the river channel. All plots show the spatial distribution of q_{Gr} at time 9000 s, when the flood peak has passed through the downstream section. A continuous inflow event is considered with $T_P = 1800\ s$, $C_3 = 2$, and $Q_P = 1000\ m^3/s$, and the downstream sampling location is 10 *km*. (a) the gamma distribution with $\overline{K} = 0.0005m/s$ and RSD = 1.5; (b) the lognormal distribution with $\overline{K} = 0.0005m/s$ and RSD = 1.5; (c) K is uniformly distributed in the lateral hyporheic zone (RSD = 0) and its mean value is $0.0005m/s$; and (d) q_{Gr} calculated from the above-mentioned different K distributions is arranged in descending order.

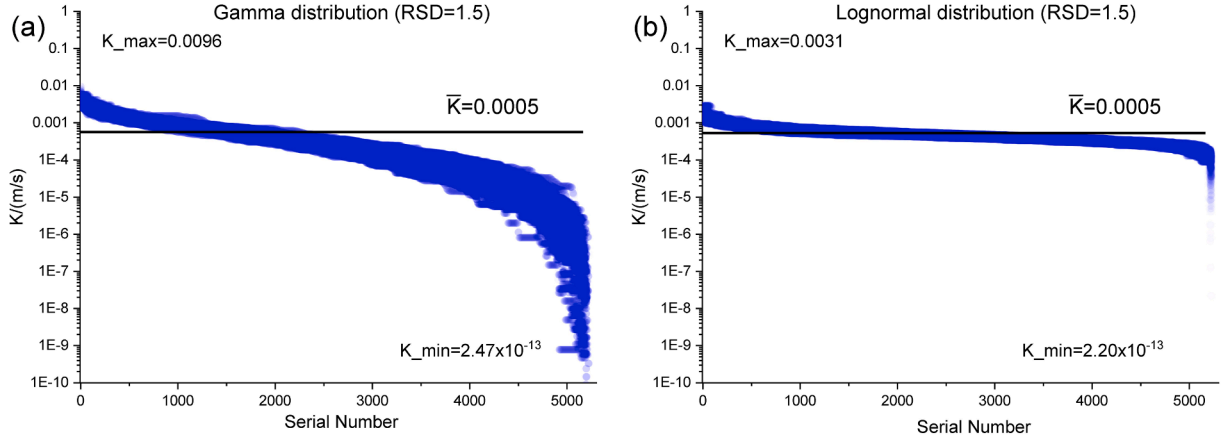

Fig. 8. The distribution range of K_i used in Fig. 5. (a) the gamma distribution with $\overline{K} = 0.0005m/s$ and RSD = 1.5; (b) the lognormal distribution with $\overline{K} = 0.0005m/s$ and RSD = 1.5. We randomly generated 100 sets of K_i, each with 5,000 values; and then ranked them from large to small and counted the proportion of these K in different ranges.

rate HEFs may be closer to the power-law decay. In conclusion, the hydrograph pattern is mainly controlled by the following factors: (1) the distribution range of K and the proportions of different distribution ranges, and (2) whether the hydrograph's peak discharge and tail portion are sensitive to K.

Some studies (Kirchner and Colin, 2013; Zhang et al., 2017) have shown that geological heterogeneity that exhibits multi-scaling behaviors can be responsible for the power-law tailing phenomenon of hydrological processes in catchments. Our study suggests that the spatially heterogeneous HEFs lead to multi-rate return flows between the riparian

Table 2
The proportion of K_i (used in Fig. 5) in different ranges generated by the lognormal distribution versus the gamma distribution with different RSDs (0.5, 1.0, and 1.5).

	Gamma distribution			Lognormal distribution		
K range (m/s)	RSD =0.5	RSD =1.0	RSD =1.5	RSD =0.5	RSD =1.0	RSD =1.5
(5E-3, 1E-1]	0.00%	0.00%	0.12%	0.00%	0.15%	0.83%
(5E-4, 5E-3]	44.26%	38.30%	32.50%	40.97%	32.35%	24.85%
(5E-5, 5E-4]	55.48%	54.47%	44.27%	58.93%	64.49%	58.01%
(5E-6, 5E-5]	0.15%	6.14	14.77%	0.04%	2.63%	15.05%
(5E-7, 5E-6]	0.00%	0.63%	5.10%	0.00%	0.01%	0.67%
(0, 5E-7]	0.11%	0.46%	3.25%	0.06%	0.37%	0.59%

zone and river, enhancing the hydrograph's late-time tail. Different hydraulic conductivity distributions within the catchment lead to different late-time tailing behaviors of the hydrograph. These interacting hydrodynamic processes in the catchment system act as a filter that smooths the input signal (e.g., inflow and chemistry) from the upstream location. In addition to the HEFs, other hydrological processes (such as nutrients moving in streams) affected by soil heterogeneity may also exhibit a power-law decay phenomenon. The modeling methods and conclusions of this work can also be extended to these hydrological processes.

5. Preliminary application

As a preliminary test, the DDCM proposed above is applied here to simulate the hydrographs induced by rainfall events in the Wadi Ahin West, Oman (Fig. 9). The hourly flow and rainfall data were obtained from the Hayl flow gauge and the seven rainfall gauges in the Wadi Ahin West catchment (*Aisha* Al-Qurashi et al., 2008). The Wadi Ahin West catchment, situated in the north of Oman, has a drainage area of 734 km^2 and low vegetation cover, with the channels in this catchment consisting mainly of sands and gravel; see *Aisha* Al-Qurashi et al. (2008) for detailed hydrologic conditions of the study site.

Nine rainfall events from 1996 to 1998 (where rainfall durations were short and concentrated) were simulated by the DDCM for the study site. These nine rainfall events were named by their dates, for example event 05 September 1998. The information of these nine rainfall events is listed in Table 3, and the field data and the model results of the nine hydrographs are plotted in Fig. 10. The width (B_r) and slope of the channels (J) in the model were defined based on the data in *Aisha* Al-Qurashi et al. (2008). The hydraulic conductivity (K) and Manining's roughness coefficient (n_c) were then calibrated: we fixed the two parameters B_r and J determined above, set different K and n_c values for simulation, and then calculated the coefficient of determination of the model results based on the field data. This trial-and-error approach led to the best-fit K and n_c with the largest coefficient of determination. The best-fit Manining's coefficient was 0.035, close to that (0.036) approximated by Aisha Al-Qurashi et al. (2008). The hydraulic conductivity K was first assumed to be uniform and isotropic to check whether the simplified model can capture the general pattern of the hydrograph; if not, then a high-resolution, heterogeneous K distribution would be fitted. The other reason for selecting a uniform K as the first fitting exercise was because of the limited hydrologic information of this study site, including for example the coarse-resolution rainfall data mentioned below (which increased the uncertainty for a fine-resolution model with a complex K distribution). We also assumed that the rainfall recharge in the riparian zones flowed mainly to the corresponding river channels (R1-R6). Notably, this assumption was not based on field observations (which were not available), but for application simplification (to reduce the number of unknown parameters). For each rainfall event simulation, the four main parameters of the DDCM (K, n_c, J, and B_r) remained unchanged (and hence the model applicability was partially validated for this study site). The time step size was set as $\Delta t = 100\,s$, and space step sizes were set as $\Delta x = 2\,m$ and $\Delta y = 50\,m$. As shown in Fig. 10, the initial river discharge of the 9 simulated rainfall-runoff events was close to base flow; hence, the initial condition was selected as base flow, and the calculated discharge was then subtracted by the initial discharge.

Considering the large basin area (~734 km^2), the spatial distribution of rainfall has a great influence on the observed hydrographs, but the actual spatial distribution of rainfall was unknown (note that the seven gauges were not enough to provide a high-resolution spatial distribution of rainfall needed for the fine-resolution model). Therefore, the following two rainfall patterns were considered to simulate the hydrographs: (1) rainfall fell evenly within the catchment (the corresponding model is abbreviated as DDCM_E), and (2) rainfall fell within a 5 km radius of the rainfall center (the corresponding model is abbreviated as DDCM_C). The model-input rainfall per unit time assigned for each subcatchment (R_i) is calculated according to the runoff coefficient, and rainfall intensity and area. Finally, based on the river network information (as shown in Fig. 9), the hydrodynamic process of each subchannel is connected to calculate the hydrograph at the downstream outlet, which is then compared with the observed hydrograph.

Fig. 10 shows the data of these nine runoff events and the results of the model simulation. In the two events "05 September 1998" and "07 August 1996" (the left two plots on the top row), although the rainfall was short and concentrated, the observed hydrograph showed a bimodal phenomenon (Fig. 10a and 10b). In this case, the simulation results of DDCM_E were better than that of DDCM_C. This may be because the rainfall events were evenly distributed in the basin and river water from

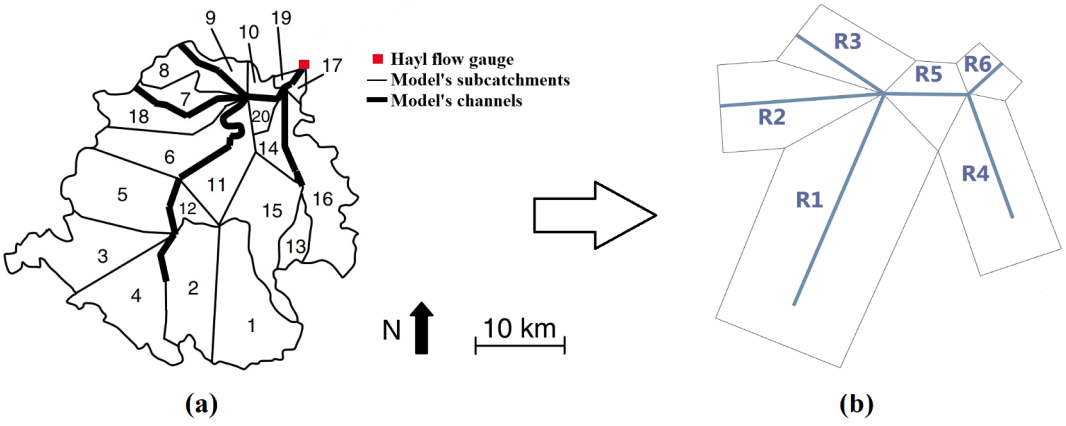

Fig. 9. (a) Schematic map of the sub-catchments and channels in the Wadi Ahin West, Oman (data from *Aisha* Al-Qurashi et al. (2008). (b) According to the catchment information shown in (a), the river network was simplified into 6 river channels and the corresponding riparian zones where the DDCM was used for simulation.

Table 3
Statistics of the runoff events (data from *Aisha* Al-Qurashi et al. (2008)).

Date	Peak gauge average rainfall (*mm/h*)	Total rainfall (*mm*)	Rainfall centroid distance from flow gauge (*km*)	Base flow (*mm/h*)	Runoff coefficient
11-Mar-1996	6	21	20	0.001	0.28
26-Jun-1996	4	5	18	0.000	0.13
07-Aug-1996	5	9	28	0.003	0.15
13-Sep-1997	3	6	25	0.003	0.13
11-Oct-1997	2	4	19	0.002	0.16
29-Oct-1997	4	9	16	0.003	0.15
17-Jul-1998	1	2	26	0.001	0.09
20-Jul-1998	7	10	25	0.001	0.13
05-Sep-1998	4	1	20	0.001	0.15

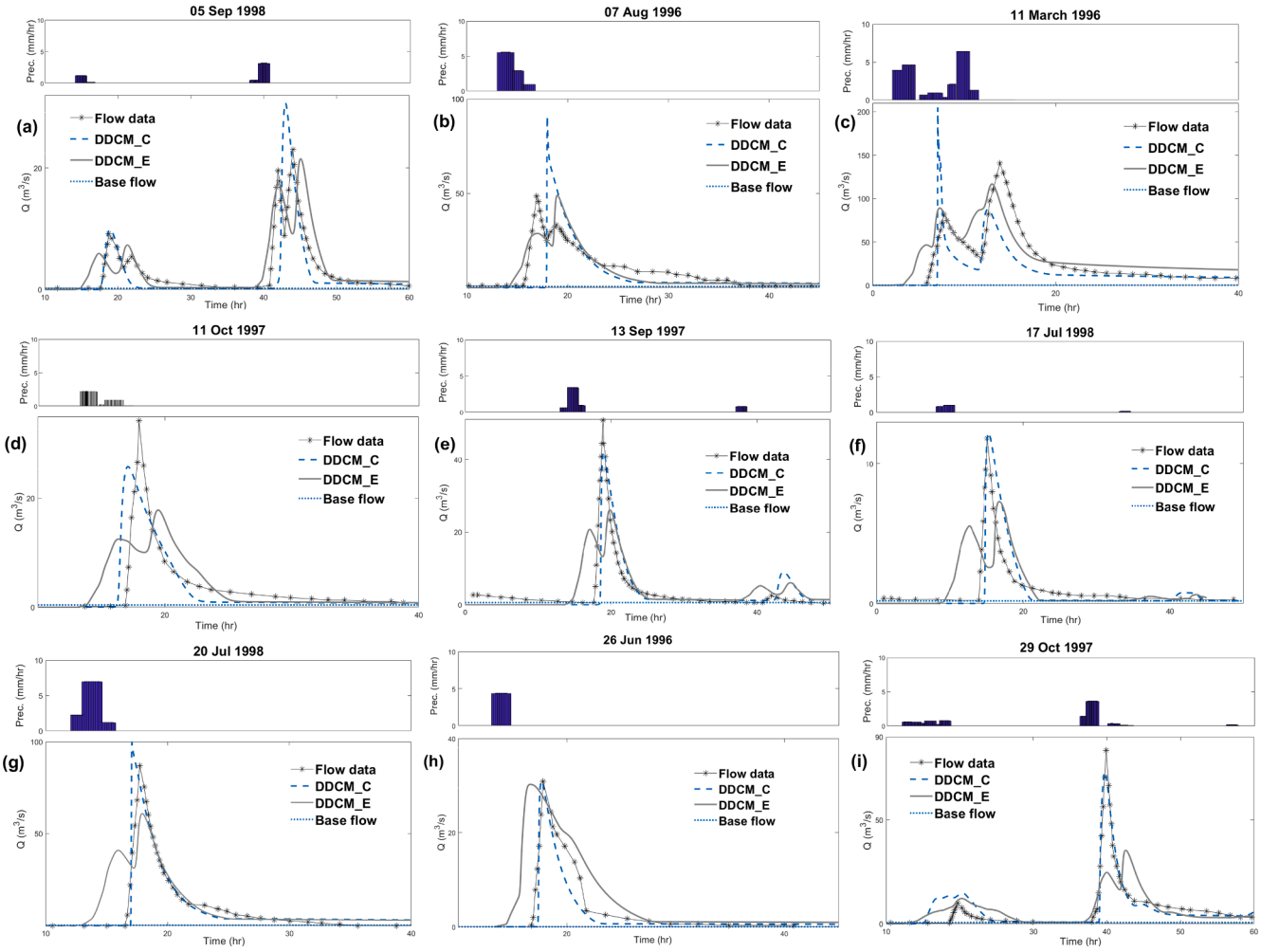

Fig. 10. Comparison of the observed hydrographs and the coupling model results (DDCM_E and DDCM_C consider two rainfall patterns, respectively) for the nine rainfall events from 1996 to 1998.

different tributaries reached downstream at different times, resulting in a bimodal peak. During the rainfall event "11 March 1996", there were two periods of relatively strong rainfall, which lead to the bimodal phenomenon (Fig. 10c). At this time, the DDCM_E hydrograph was closer to the observed one, but the model fit was still not satisfactory, implying the complex spatiotemporal distribution of this rainfall event. For other rainfall events (such as 11 October 1997, 13 September 1997, 17 July 1998, 20 July 1998, and 29 October 1997; see Fig. 9e–9i), one flood peak was detected downstream. The simulation results of DDCM _C were closer to the observed data than those of DDCM _E. This indicates that the actual rainfall distribution might be concentrated near the rainfall centers, while there was little rainfall in the tributary sub-catchments. Table 4 shows the coefficient of determination (R^2) and the Nash-Sutcliffe efficiency (NSE) coefficient of the 9 rainfall events. Because DDCM is a physical process-based model, it is sensitive to input conditions (rainfall distribution). When the rainfall distribution is known, the DDCM can describe the downstream hydrograph.

As shown in Fig. 9a, the real river has several curved sections, and hence the simplification of the river network to the straight channel shown in Fig. 9b may affect the simulation results in at least two ways. First, compared with straight channels, water flow slows downstream in the curved ones. Therefore, the peak arrival time in the hydrograph simulated by the DDCM may be biased. Second, the magnitude and pattern of HEFs along the curved channel are different from those along the straight channel (Storey et al., 2003; Boano et al., 2006; Allgeier et al., 2021; Morén et al., 2021). Especially in the upstream part of the

Table 4
Performance of the two DDCMs for the 9 rainfall-runoff events shown in Fig. 10. Considering two rainfall distributions (simulated by DDCM_C and DDCM_E, respectively), the coefficient of determination (R^2) and the Nash-Sutcliffe efficiency (NSE) coefficient of the results were calculated. Highlighted font indicates the better selection of rainfall distribution in the model.

Date	5-Sep-98		7-Aug-96		11-Mar-96	
Model	DDCM_C	DDCM_E	DDCM_C	DDCM_E	DDCM_C	DDCM_E
R^2	0.4228	0.6081	0.2287	0.7809	0.3561	0.5578
NSE	−0.0187	0.5473	−0.4545	0.7520	0.0897	0.0561
Date	11-Oct-97		13-Sep-97		17-Jul-98	
Model	DDCM_C	DDCM_E	DDCM_C	DDCM_E	DDCM_C	DDCM_E
R^2	0.4588	0.2861	0.6790	0.4673	0.6311	0.3119
NSE	0.3044	0.2697	0.6602	0.4388	0.4054	0.1274
Date	20-Jul-98		26-Jun-96		29-Oct-97	
Model	DDCM_C	DDCM_E	DDCM_C	DDCM_E	DDCM_C	DDCM_E
R^2	0.8384	0.7859	0.8449	0.3951	0.9259	0.4691
NSE	0.7770	0.7795	0.7717	−0.4541	0.9191	0.4666

curved channel, the water pressure is high, which will promote the HEFs to enter the riparian zone, and part of the HEFs will reach the downstream through the curved riparian zone. These factors will affect the hydrograph pattern and need to be systematically evaluated in a future study using a field site with a finer resolution of hydrologic data.

Notably, this preliminary application only checked the applicability of the DDCM in simplifying complex river dynamics. Further applications are still needed to evaluate the DDCM's full capability in quantifying the impacts of the lateral HEF and the aquifer heterogeneity on the nuance of the real-world hydrograph (especially its peak and tail).

It is also noteworthy that the impact of HEFs on the hydrograph cannot be neglected in flood events, although the rate of HEFs can be several orders of magnitude lower than the flood discharge. Previous studies showed that the rate of lateral HEFs significantly increased during flood events (Liu et al., 2020) and the HEFs occurred throughout the river network (Kiel and Cardenas, 2014). The DDCM proposed by this study considered the influence of lateral HEFs on hydrograph. Our numerical results revealed the buffering effect of lateral HEFs on flood hydrograph, where the magnitude of this buffering effect is related to the riverbank sediment hydraulic conductivity, channel characteristics, and flow conditions. As the flood flows over a long distance, the river water is continuously forced to enter riparian zones, and this accumulative discharge loss needs to be considered especially when K is large. Calculations in Fig. 10 also considered the effect of lateral HEFs; otherwise, the model results would fit worse the observed hydrographs.

5.1. Influence of model parameters on rainfall runoff

The above-mentioned simulations revealed that input conditions (rainfall or upstream flood) in the HEFs have dissimilar impacts on the resultant hydrograph pattern. When the rainfall starts, the initial river flow mainly consists of the rain that falls directly on the river surface and the amount of water that enters the channel rapidly. After the rainfall event, the flow in the channel is recharged by HEFs, which have a certain influence on the river discharge and flow velocity. When the upstream flood arrives, HEFs can reduce the flood peak value and cause hydrograph tailing behavior. However, due to the large flood discharge and fast flow velocity, the influence of HEFs on flood velocity is limited. Based on the river channel data in Section 5 (shown in Fig. 9), we investigated the effects of the four DDCM parameters (K, B_r, J, and n_c) on hydrograph under rainfall condition. The simulation results are shown in Fig. 11, where base flow was subtracted from the river discharge.

As shown in Fig. 11a, the increase of K increases the rate of HEFs, which reduces the discharge peak and causes the hydrograph tailing behavior. In contrast to the flood condition, the hydrograph tail is smoother and lasts longer under the rainfall condition. The reason is that the rain falls directly on the riparian zone and raises the groundwater table, which can provide long-term HEFs. Fig. 11b shows that an increase of B_r may lead to a decrease in the mean flow velocity, which is different from the results shown in Fig. 3b. In this example, the effect of rainfall was to raise the river stage and the hydraulic head of groundwater. According to the Manning's formula ($u_r = \frac{1}{n_c}R^{2/3}J^{1/2}$, $R = \frac{B_r \bullet h_r}{B_r + 2h_r}$), when h_r is the same, the larger the B_r, the faster the river flow. After the rainfall, groundwater began to recharge the river, and the wider the river channel, the smaller the river stage rise caused by the same HEFs. This means that a larger channel width leads to a larger river flow velocity during the rainfall period, while the river flow velocity with a wider channel will decline faster after the rainfall. In this example, the rainfall center is 25 km away from the downstream section. The simulation results showed that a larger river width led to a longer time for the flow peak to reach the downstream section. As shown in Fig. 11c, J has a great influence on the flow velocity under the rainfall condition, as expected. Contrarily, for the case of upstream flood (Fig. 3c), J has a limited influence on the flow velocity. As shown in Fig. 11d, a large n_c reduces the peak discharge and increases the peak arrival time, which is consistent with the results under the upstream flood condition. In conclusion, the influence of HEFs on hydrograph is not only related to hydrogeological parameters, but also to the flow and rainfall conditions.

It is also noteworthy that the hydrograph can be influenced by many factors, in addition to the spatial and temporal distribution of rainfall, the soil moisture and heterogeneity, and the characteristics of the channel, etc. Because the DDCM cannot capture the nuance of these factors, it is difficult for DDCM to accurately predict the hydrograph. The accuracy of experimental data also affects the model results. For example, the water surface slope data for each tributary only has an average value, limiting the DDCM's capability in modeling the nuance of discharge. However, the DDCM can quickly predict the overall pattern of the hydrograph with limited hydrological data, which can be practically useful for the field sites at a large scale with limited hydrological information.

6. Conclusion

This study proposed a distributed-domain model (DDCM) by coupling the river dynamic process and the hydrologic exchange process to quantify the influence of bidirectional hydrologic exchange flows (HEFs) on hydrograph patterns. A series of numerical experiments were conducted using a synthetic river-aquifer case. The influence of the channel characteristics, including the sediment hydraulic conductivity K, the river channel width B_r, the hydraulic gradient J, and the channel roughness n_c on hydrograph patterns were analyzed. Moreover, the impact of the hydraulic conductivity distribution on the falling limb of streamflow response was investigated, by explicitly accounting for the heterogeneity in K. The present DDCM was then applied to characterize the observed hydrographs. The major conclusions of this study are as follows.

First, the lateral HEF can have a buffering effect on flood routing and at the same time cause the tailing phenomenon of the flood process. The flow rate of lateral HEF is mainly controlled by K. When K is large, the hydrologic exchange rate increases, and the flood peak is significantly reduced. Meanwhile, a large K leads to a heavy hydrograph tailing behavior at the late time with a short duration. River channel characteristics including n_c, J, and B_r have a great influence on the downstream hydrograph. The downstream flood encounters a greater dissipation with an increasing n_c and decreasing J and B_r. These findings can be important for flood control.

Second, the spatial heterogeneity in K can have a significant impact on the shape of the hydrograph. In general, as the RSD of K increases, the late-time hydrograph tends to exhibit a power-law decline because the spatially heterogeneous HEFs between the riparian zone and the river channel can lead to multi-rate return flows. The hydrograph tailing behavior is mainly controlled by the following two factors: (1) the

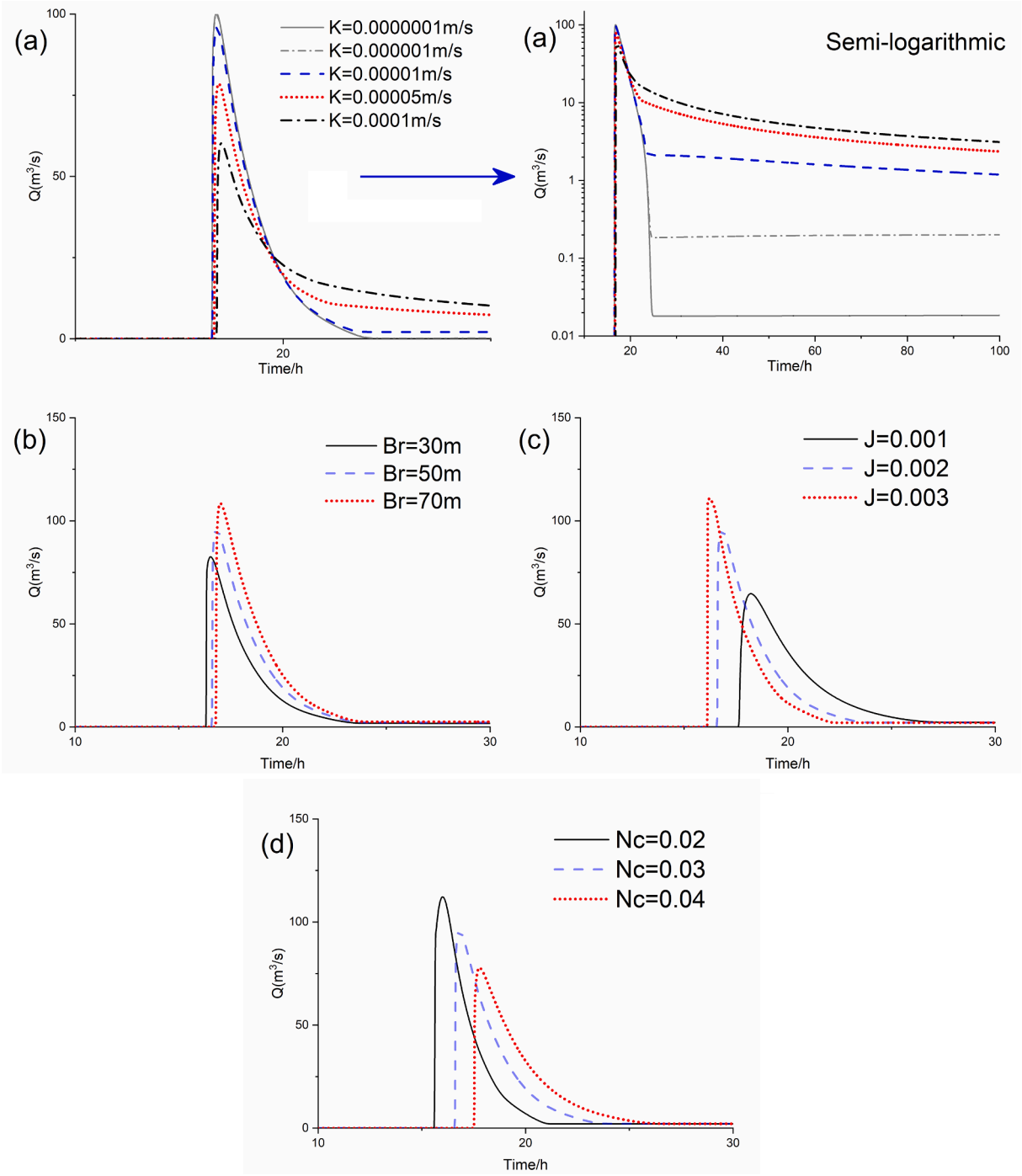

Fig. 11. The influence of parameter variation (i.e., K, B_r, J, and n_c) on the hydrograph pattern (Q_r). The river channel characteristics were the same as those used in Fig. 10, and the rainfall conditions were set in accordance with the event "20 July 1998", and the rainfall was assumed to fall within a 5 *km* radius of the rainfall center. Base flow was subtracted from the hydrograph shown in this figure. The default values of the DDCM parameters were $K = 0.00001\ m/s$, B_r=50 *m*, $J = 0.002$, and $n_c = 0.03$.

distribution range of K and the proportions of different distribution ranges, and (2) the sensitivity of hydrograph pattern to the variation of K. This is the major mechanism of the power-law tailing behavior of hydrographs revealed by this study.

Third, the influence of HEFs to the hydrograph pattern is related to the channel characteristics, the riparian zone permeability, flow conditions, and the spatiotemporal distribution of rainfall.

Fourth, the DDCM proposed by this study can simulate the flood hydrographs observed at the Hayl flow gauge in the Wadi Ahin West, Oman. The rainfall distribution in the basin has a great influence on the hydrograph pattern. It was expected that, if the rainfall distribution can be reasonably captured, DDCM may characterize better the observed hydrograph pattern. Further applications are needed to check the applicability of the DDCM in quantifying the impacts of the lateral HEF and the aquifer heterogeneity on the nuance of real-world hydrographs.

CRediT authorship contribution statement

Song Wei: Methodology, Software, Validation, Writing – original draft, Visualization, Writing – review & editing. **Yi Zheng:**

Conceptualization, Supervision, Investigation, Writing – original draft. **Xiuyu Liang:** Methodology, Software. **Peng Xu:** Methodology. **Yong Tian:** Methodology. **Jonathan Frame:** Writing – review & editing. **Yong Zhang:** Conceptualization, Supervision, Investigation, Writing – original draft, Writing – review & editing.

Declaration of Competing Interest

The authors declare that they have no known competing financial interests or personal relationships that could have appeared to influence the work reported in this paper.

Acknowledgments

This work was supported by the Shenzhen Science and Technology Innovation Commission (No. KCXFZ202002011006491), the National Natural Science Foundation of Guangxi Province, China (Grant No. 2020GXNSFBA297038), and the National Natural Science Foundation of China (No. 51961125203; No. 41931292). Y.Z. was partially funded by the Alabama Center of Excellence (ALCoE, GR28628). Data is available through Aisha Al-Qurashi et al. (2008).

Appendix A. Numerical approach for solving the proposed DDCM model

As shown in Fig. 2, the DDCM model simplified the river-riparian system into a coupled 1D river channel and 2D groundwater hydrodynamic process. Due to the symmetry of both sides of the river, only the riparian zone on one side needs to be calculated here, although the hyporheic exchange on both sides of the river needs to be considered when quantifying the river flow hydrodynamics. The river channel is divided into N sections ($N = L/\Delta y$), and the riparian zone is divided into $N \times M$ sub-areas (where $M = b/\Delta x$), where Δx and Δy are the spatial step sizes in the x- and y-directions, respectively. The total time of the model simulation is denoted as T, and the total time step is $N_t = T/\Delta t$, where Δt is the time interval. For simplification, here we use superscripts to denote time and subscripts to denote space. For example, $Z_{r_j}^{\ k}$ represents the numerical result of the river stage Z_r at time $k\Delta t$ and position $y = j\Delta y$, and $H_{G_{i,j}}^{k}$ represents the numerical result of the groundwater hydraulic head H_G at time $k\Delta t$ and position $(x, y) = (i\Delta x, j\Delta y)$.

The DDCM model is solved numerically using the following three steps:

Step I: Based on the water level information (h^k, ${Z_r}^k$, and ${H_G}^k$) of the river channel and the riparian zone at the k-th time step ($k = 1, \cdots, N_t - 1$), the hydrologic exchange flux (${q_{Gr}}^k = (Kh)^k\left({H_G}^k - {Z_r}^k\right)/\Delta x$) is calculated.

Step II: The water level of the river channel (${Z_r}^{k+1}$) at the $(k+1)$-th time step can be obtained by solving the open channel flow model (Eq. (2)) according to the Preissmann scheme (Lyn and Goodwin, 1987); Using the ADI method to solve the groundwater flow model (Eq. (3)), the groundwater level data (h^{k+1} and ${H_G}^{k+1}$) at the $(k+1)$-th time step can be obtained (Xue and Xie, 2007).

Step III: The water level data calculated in Step II (i.e., h^{k+1}, ${Z_r}^{k+1}$, and ${H_G}^{k+1}$) are used to recalibrate the hydrologic exchange flux (${q_{Gr^*}}^k$). Repeat Step II to gain the corrected water level of river and riparian zone (${Z_{r^*}}^{k+1}$ and ${H_{G^*}}^{k+1}$). Calculate the relative error between the original water levels and the corrected ones, i.e., $\varepsilon_1 = \left|{Z_{r^*}}^{k+1} - {Z_r}^{k+1}\right|/{Z_r}^{k+1}$ and $\varepsilon_2 = \left|{H_{G^*}}^{k+1} - {H_G}^{k+1}\right|/{H_G}^{k+1}$. If one of the relative errors is greater than the convergence criteria ($\varepsilon_1 \gg \varepsilon_{0,1}$, or $\varepsilon_2 \geq \varepsilon_{0,2}$), the iteration continues. If the relative errors are less than the convergence criteria ($\varepsilon_1 < \varepsilon_{0,1}$, and $\varepsilon_2 < \varepsilon_{0,2}$), the numerical result is considered to be stable, and then move to Step 1 to solve the next time step.

The following part describes the difference equation after applying the finite different approach for the open channel flow model (i.e., Saint Venant equation) and the groundwater flow model (Boussinesq equation).

(a) The Preissmann scheme for Saint Venant equation.

The variables in equation (2) and their partial derivatives are approximated by:

$$f \approx \frac{\theta\left(f_{j+1}^{n+1} + f_j^{n+1}\right) + (1-\theta)\left(f_{j+1}^{n} + f_j^{n}\right)}{2}$$

$$\frac{\partial f}{\partial x} \approx \frac{\theta\left(f_{j+1}^{n+1} - f_j^{n+1}\right) + (1-\theta)\left(f_{j+1}^{n} - f_j^{n}\right)}{\Delta x}$$

$$\frac{\partial f}{\partial t} \approx \frac{\left(f_{j+1}^{n+1} + f_j^{n+1}\right) - \left(f_{j+1}^{n} + f_j^{n}\right)}{2\Delta t}$$

and we define

$$f_{j+1/2}^{n} = \left(f_j^{n} + f_{j+1}^{n}\right)/2$$

where θ is the weighting parameter (an explicit format is formed when $\theta = 0$, and an implicit is formed when $\theta \geq 0.5$). In this study, we set $\theta = 0.5$. Therefore, equation (2a) can be discretized into the following form:

$$B_{r_{j+1/2}}^{\ n} \frac{\left(Z_{r_{j+1}}^{\ n+1} + Z_{r_j}^{\ n+1}\right) - \left(Z_{r_{j+1}}^{\ n} + Z_{r_j}^{\ n}\right)}{2\Delta t} + \frac{\theta\left(Q_{j+1}^{n+1} - Q_j^{n+1}\right) + (1-\theta)\left(Q_{j+1}^{n} - Q_j^{n}\right)}{\Delta x} = {q_{L_j}}^n + {q_{Gr_j}}^n$$

Further arrangement leads to

$$-Q_j^{n+1} + C_j Z_{r_j}^{\ n+1} + Q_{j+1}^{n+1} + C_j Z_{r_{j+1}}^{\ n+1} = D_j \tag{A1}$$

where $C_j = \frac{\Delta x}{2\theta\Delta t} B_{r_{j+1/2}}^{\ n}$, $D_j = \frac{\Delta x}{\theta}\left({q_L}_j^n + {q_{Gr}}_j^n\right) + \frac{1-\theta}{\theta}\left(Q_j^n - Q_j^{n+1}\right) + C_j\left(Z_{r_{j+1}}^{\ n} + Z_{r_j}^{\ n}\right)$. ${q_L}_j^n$ is known, and ${q_{Gr}}_j^n = (Kh)_j^n\left(H_{G_j}^{\ n} - Z_{r_j}^{\ n}\right)/\Delta x$.

Equation (2b) can be discretized as

$$\frac{Q_{j+1}^{n+1}+Q_j^{n+1}-Q_{j+1}^{n}-Q_j^{n}}{2\Delta t}+2u_{r_{j+1/2}}^{n}\frac{\theta\left(Q_{j+1}^{n+1}-Q_j^{n+1}\right)+(1-\theta)\left(Q_{j+1}^{n}-Q_j^{n}\right)}{\Delta y}+\left(gA_r-Bu_r^2\right)_{j+1/2}^{n}\frac{\theta\left(Z_{r_{j+1}}^{n+1}-Z_{r_j}^{n+1}\right)+(1-\theta)\left(Z_{r_{j+1}}^{n}-Z_{r_j}^{n}\right)}{\Delta y}$$
$$-\left(u_r^2\frac{\partial A}{\partial y}\Big|_{Z_r=const}\right)_{j+\frac{1}{2}}^{n}+\frac{g}{2}\left(\frac{A_r}{k_r^2}\right)_j^{n}\left|Q_j^{n}\right|Q_j^{n+1}+\frac{g}{2}\left(\frac{A_r}{k_r^2}\right)_{j+1}^{n}\left|Q_{j+1}^{n}\right|Q_{j+1}^{n+1}=0$$

where $k_r=A_rC\sqrt{R}$, C is the Chézy coefficient, and R denotes the hydraulic radius.

Further rearrangement leads to.

$$E_jQ_j^{n+1}-F_jZ_{r_j}^{n+1}+G_jQ_{j+1}^{n+1}+F_jZ_{r_{j+1}}^{n+1}=\phi_j \tag{A2}$$

where

$$E_j=\frac{\Delta y}{2\theta\Delta t}-2u_{r_{j+\frac{1}{2}}}^{n}+\frac{g\Delta y}{2\theta}\left(\frac{A_r|Q|}{k_r^2}\right)_j^{n}$$

$$G_j=\frac{\Delta y}{2\theta\Delta t}+2u_{r_{j+\frac{1}{2}}}^{n}+\frac{g\Delta y}{2\theta}\left(\frac{A_r|Q|}{k_r^2}\right)_{j+1}^{n}$$

$$F_j=\left(gA_r-Bu_r^2\right)_{j+1/2}^{n}$$

$$\phi_j=\frac{\Delta y}{2\theta\Delta t}\left(Q_{j+1}^{n}+Q_j^{n}\right)+\frac{2(1-\theta)}{\theta}u_{r_{j+\frac{1}{2}}}^{n}\left(Q_j^{n}-Q_{j+1}^{n}\right)+\frac{1-\theta}{\theta}\left(gA_r-Bu_r^2\right)_{j+1/2}^{n}\left(Z_{r_j}^{n}-Z_{r_{j+1}}^{n}\right)+\frac{\Delta y}{\theta}\left(u_r^2\frac{\partial A}{\partial y}\Big|_{Z_r=const}\right)_{j+\frac{1}{2}}^{n}$$

Applying equations (A1) and (A2) and the initial and boundary conditions, we can build a matrix to solve the river dynamic process.

(b) The ADI scheme for 2D Boussinesq equation.

The ADI scheme assumes an intermediate time step $t_{i+1/2}$ between t_i and t_{i+1}. The algorithm contains two steps. Step 1: from t_i to $t_{i+1/2}$, the discretization of the governing equation in the x direction adopts the implicit finite difference scheme, while the discretization in the y direction adopts the explicit finite difference scheme. Step 2: from $t_{i+1/2}$ to t_{i+1}, the explicit and implicit finite difference schemes are used to discretize the governing equation in the x direction and y direction, respectively.

For the discretization of equation (3), the derivative is replaced by the following difference quotient form:

$$\frac{\partial}{\partial x}\left(Kh\frac{\partial H_G}{\partial x}\right)\Big|_{i,j}=\frac{1}{\Delta x}\left[\left(Kh\frac{\partial H_G}{\partial x}\right)\Big|_{i+\frac{1}{2},j}-\left(Kh\frac{\partial H_G}{\partial x}\right)\Big|_{i-\frac{1}{2},j}\right]+O\left([\Delta x]^2\right)\approx(Kh)_{i+\frac{1}{2}j}\frac{H_{Gi+1,j}-H_{Gi,j}}{(\Delta x)^2}+(Kh)_{i-\frac{1}{2}j}\frac{H_{Gi-1,j}-H_{Gi,j}}{(\Delta x)^2}$$

where $(Kh)_{i+\frac{1}{2}j}$ and $(Kh)_{i-\frac{1}{2}j}$ represent the Kh value at node $\left(\left(i+\frac{1}{2}\right)\Delta x,j\Delta y\right)$ and node $\left(\left(i-\frac{1}{2}\right)\Delta x,j\Delta y\right)$, respectively.

If the aquifer heterogeneity is strong, the following approximation (harmonic mean approximation) can be used (Xue and Xie, 2007):

$$(Kh)_{i+\frac{1}{2}j}=\frac{2K_{i,j}\bullet K_{i+1,j}}{K_{i,j}+K_{i+1,j}}\sqrt{h_{i,j}\bullet h_{i+1,j}}$$

$$(Kh)_{i-\frac{1}{2}j}=\frac{2K_{i,j}\bullet K_{i-1,j}}{K_{i,j}+K_{i-1,j}}\sqrt{h_{i,j}\bullet h_{i-1,j}}$$

$$(Kh)_{i,j+1/2}=\frac{2K_{i,j}\bullet K_{i,j+1}}{K_{i,j}+K_{i,j+1}}\sqrt{h_{i,j}\bullet h_{i,j+1}}$$

$$(Kh)_{i,j-1/2}=\frac{2K_{i,j}\bullet K_{i,j-1}}{K_{i,j}+K_{i,j-1}}\sqrt{h_{i,j}\bullet h_{i,j-1}}$$

First, from t_i to $t_{i+1/2}$, the discretization form of the governing equation (3a) is as follows:

$$\frac{(Kh)_{i-1/2,j}^{n}}{\Delta x^2}H_{Gi-1,j}^{n+1}+\left(-\frac{2S_y}{\Delta t}-\frac{(Kh)_{i+1/2,j}^{n}}{\Delta x^2}-\frac{(Kh)_{i-1/2,j}^{n}}{\Delta x^2}\right)H_{G\,i,j}^{n+1}+\frac{(Kh)_{i+1/2,j}^{n}}{\Delta x^2}H_{Gi+1,j}^{n+1}=-\frac{2S_y}{\Delta t}H_{G\,i,j}^{n}-W_{i,j}^{n}\Delta x\Delta y-(Kh)_{i,j+1/2}^{n}\frac{H_{Gi,j+1}^{n}-H_{Gi,j}^{n}}{\Delta y^2}-(Kh)_{i,j-1/2}^{n}\frac{H_{Gi,j-1}^{n}-H_{Gi,j}^{n}}{\Delta y^2} \tag{A3}$$

The numerical solution at time $t_{i+1/2}$ can be obtained by solving equation (A3).

Next, from $t_{i+1/2}$ to t_{i+1}, the discretization form of the governing equation (3a) is as follows:

$$\frac{(Kh)_{i,j-1/2}^{n}}{\Delta y^2}H_{Gi,j-1}^{n+1}+\left(-\frac{2S_y}{\Delta t}-\frac{(Kh)_{i,j+1/2}^{n}}{\Delta y^2}-\frac{(Kh)_{i,j-1/2}^{n}}{\Delta y^2}\right)H_{G\,i,j}^{n+1}+\frac{(Kh)_{i,j+1/2}^{n}}{\Delta y^2}H_{Gi,j+1}^{n+1}=-\frac{2S_y}{\Delta t}H_{G\,i,j}^{n}-W_{i,j}^{n}\Delta x\Delta y-(Kh)_{i+1/2,j}^{n}\frac{H_{Gi+1,j}^{n}-H_{Gi,j}^{n}}{\Delta x^2}-(Kh)_{i-1/2,j}^{n}\frac{H_{Gi-1,j}^{n}-H_{Gi,j}^{n}}{\Delta x^2} \tag{A4}$$

Therefore, the water level distribution of the riparian zone at time t_{i+1} can finally be obtained by solving equation (A4).

Appendix B. Numerical strategy for calculating the catchment-scale hydrograph with rainfall events using DDCM

When applying the DDCM method proposed by this study to calculate the hydrograph for a catchment, the sub-domain discretization and related hydrologic calculations are needed. To reach this goal, we proposed the following two-step numerical strategy and applied it for solving the catchment-scale hydrography with rainfall events in the Wadi Ahin West catchment shown in section 5.

Step I: Catchment separation and rainfall data processing.

(1) Based on the characteristics of the river network (mainly the sub-drainage delineation), the catchment is divided into sub-domains.

(2) The rainfall received by each sub-catchment is then calculated according to the intensity and spatial distribution of the rainfall and the area of the sub-catchment. These rainfall results are then allocated to each sub-domain underlying each sub-catchment.

For example, for the Wadi Ahin West catchment discussed in Section 5, six sub-domains were identified and named as R1–R6 in Fig. 9b, each of which contains the corresponding sub-catchments (No. 1–20 shown in Fig. 9a). Specifically, sub-domain R1 contains sub-catchments 2–6, 11, and 12. Sub-domain R2 contains sub-catchments 7 and 18. Sub-domain R3 contains sub-catchments 8 and 9. Sub-domain R4 contains sub-catchments 1, and 13–16. Sub-domain R5 contains sub-catchments 10 and 20, and sub-domain R6 contains sub-catchments 17 and 19. The channel and riparian zones in each sub-domain were discretized according to the method described in **Appendix A**.

Step 2: Hydrodynamic calculation of the river network.

For a dendritic drainage basin such as the Wadi Ahin West catchment, the hydrodynamic process of the tributaries is calculated first, and then the mainstream. During this calculation, flows at the upstream channels are calculated first, followed by the downstream channels. Meanwhile, the discharge and water level at river confluences should satisfy the consistency equation.

For the Wadi Ahin West catchment, hydrodynamic calculations for the 6 sub-domains plotted in Fig. 9b were not independent but following Step 2 mentioned above. We also assumed that these six sub-domains did not exchange water at the boundary with each other, since field data about the possible water exchange between these sub-domains were not available. We emphasize here that the example shown in Section 5 was mainly to check whether the DDCM method can roughly predict the hydrograph with limited field information. An updated, robust model can be built if the core hydrologic data are available for the study basin.

References

Åkesson, A., Wörman, A., Bottacin-Busolin, A., 2015. Hydraulic response in flooded stream networks. Water Resour. Res. 51 (1), 213–240.

Allgeier, J., Martin, S., Cirpka, O.A., 2021. Systematic evaluation of geometry-driven lateral river-groundwater exchange in floodplains. Water Resour. Res. 57, e2021WR030239.

Al-Qurashi, A., Mcintyre, N., Wheater, H., Unkrich, C., 2008. Application of the Kineros2 rainfall-runoff model to an arid catchment in Oman. J. Hydrol. 355 (1–4), 91–105.

Anibas, C., Buis, K., Verhoeven, R., Meire, P., Batelaan, O., 2011. A simple thermal mapping method for seasonal spatial patterns of groundwater–surface water interaction. J. Hydrol. 397 (1–2), 93–104.

Baartman, J.E.M., Jetten, V.G., Ritsema, C.J., De Vente, J., 2012. Exploring effects of rainfall intensity and duration on soil erosion at the catchment scale using openLISEM: Prado catchment, SE Spain. Hydrol. Process. 26 (7), 1034–1049.

Bernard-Jannin, L., Brito, D., Sun, X., Jauch, E., Neves, R., Sauvage, S., Sanchez-Perez, J., 2016. Spatially distributed modelling of surface water-groundwater exchanges during overbank flood events – a case study at the Garonne River. Adv. Water Resour. 94, 146–159.

Boano, F., Camporeale, C., Revelli, R., Ridolfi, L., 2006. Sinuosity-driven hyporheic exchange in meandering rivers. Geophys. Res. Lett. 33 (18), 273–274.

Boano, F., Harvey, J.W., Marion, A., Packman, A.I., Revelli, R., Ridolfi, L., Worman, A., 2014. Hyporheic flow and transport processes: Mechanisms, models, and biogeochemical implications. Res. Geophys. 52 (4), 603–679.

Brunke, M., Gonser, T.O.M., 1997. The ecological significance of exchange processes between rivers and groundwater. Freshwater Biol. 37 (1), 1–33.

Cardenas, M.B., Wilson, J.L., Zlotnik, V.A., 2004. Impact of heterogeneity, bed forms, and stream curvature on subchannel hyporheic exchange. Water Resour. Res. 40, W08307.

Cardenas, M.B., 2008. Surface water-groundwater interface geomorphology leads to scaling of residence times. Geophys. Res. Lett. 35 (8), 307–315.

Cardenas, M.B., 2009a. A model for lateral hyporheic flow based on valley slope and channel sinuosity. Water Resour. Res. 45, W01501. https://doi.org/10.1029/2008WR007442.

Cardenas, M.B., 2009b. Stream-aquifer interactions and hyporheic exchange in gaining and losing sinuous streams. Water Resour. Res. 45 (6), 267–272.

Doble, R., Brunner, P., Mccallum, J., Cook, P.G., 2012. An analysis of river bank slope and unsaturated flow effects on bank storage. Groundwater. 50 (1), 77–86.

Dudley-Southern, M., Binley, A., 2015. Temporal responses of groundwater-surface water exchange to successive storm events. Water Resour. Res. 51 (2), 1112–1126.

Francis, B.A., Francis, L.K., Cardenas, M.B., 2015. Water table dynamics and groundwater-surface water interaction during filling and draining of a large fluvial island due to dam-induced river stage fluctuations. Water Resour. Res. 46 (7), 7513.

Gomez-Velez, J.D., Wilson, J.L., Cardenas, M.B., Harvey, J.W., 2017. Flow and residence times of dynamic river bank storage and sinuosity-driven hyporheic exchange. Water Resour. Res. 53 (10), 8572–8595.

Haggerty, R., Wondzell, S.M., Johnson, M.A., 2002. Power-law residence time distribution in the hyporheic zone of a 2nd-order mountain stream. Geophys. Res. Lett. 29 (13), 1640. https://doi.org/10.1029/2002GL014743.

Harvey, J., Gooseff, M., 2015. River corridor science: hydrologic exchange and ecological consequences from bed forms to basins. Water Resour. Res. 51 (9), 6893–6922.

Harvey, J.W., Bencala, K.E., 1993. The Effect of streambed topography on surface-subsurface water exchange in mountain catchments. Water Resour. Res. 29 (1), 89–98.

Hunt, B., 1990. An approximation for the bank storage effect. Water Resour. Res. 26 (11), 2769–2775.

Jencso, K.G., Mcglynn, B.L., Gooseff, M.N., Bencala, K.E., Wondzell, S.M., 2010. Hillslope hydrologic connectivity controls riparian groundwater turnover: implications of catchment structure for riparian buffering and stream water sources. Water Resour. Res. 46 (10), 5613–5618.

Jiang, W., Song, J., Zhang, J., Wang, Y., Zhang, N., Zhang, X., Long, Y., Li, J., Yang, X., 2015. Spatial variability of streambed vertical hydraulic conductivity and its relation to distinctive stream morphologies in the Beiluo River, Shaanxi Province, China. China. Hydrogeol. J. 23 (7), 1617–1626.

Jones, J.B., Mulholland, P.J., 1999. Streams and Ground Waters. Elsevier.

Jung, M., Burt, T.P., Bates, P.D., 2004. Toward a conceptual model of floodplain water table response. Water Resour. Res. 40, W12409.

Kiel, B.A., Cardenas, M.B., 2014. Lateral hyporheic exchange throughout the Mississippi River network. Nat. Geosci. 7 (6), 413–417.

Kirchner, J.W., Feng, J.W., Neal, X., 2000. Fractal stream chemistry and its implications for contaminant transport in catchments. Nature 403 (6769), 524–527.

Kirchner, J.W., Colin, N., 2013. Universal fractal scaling in stream chemistry and its implications for solute transport and water quality trend detection. Proc. Natl. Acad. Sci. U.S.A. 110 (30), 12213–12218.

Kollet, S.J., Maxwell, R.M., 2008. Demonstrating fractal scaling of baseflow residence time distributions using a fully-coupled groundwater and land surface model. Geophys. Res. Lett. 35 (35), 154–162.

Krause, S., Hannah, D.M., Fleckenstein, J.H., Heppell, C.M., Kaeser, D., Pickup, R., Pinay, G., Robertson, A.L., Wood, P.J., 2011. Inter-disciplinary perspectives on processes in the hyporheic zone. Ecohydrology. 4 (4), 481–499.

Lapidus, L., Pinder, G.F., 1999. Numerical Solution of Partial Differential Equations in Science and Engineering. Wiley, Wiley-Interscience, New York.

Liang, X., Zhan, H., Schilling, K., 2018. Spatiotemporal responses of groundwater flow and aquifer-river exchanges to flood events. Water Resour. Res. 54 (3), 1513–1532.

Liang, X., Zlotnik, V., Zhang, Y.K., Xin, P., 2020. Diagnostic analysis of bank storage effects on sloping floodplains. Water Resour. Res. 56(2), e2019WR026385 https://doi.org/10.1029/2019WR026385.

Liu, D., Jiang, Q., Shi, W., Chen, Q., Lee, J.Y., 2020. Hyporheic exchange mechanism driven by flood wave. Hydrol. Process. 34, 5429–5440. https://doi.org/10.1002/hyp.13956.

Lyn, D.A., Goodwin, P., 1987. Stability of a general Preissmann scheme. J. Hydraul. Eng. 113 (1), 16–28.

Morén, I., Riml, J., Wörman, A., 2021. Cross-validating hydromechanical models and tracer test assessments of hyporheic exchange flow in streams with different hydromorphological characteristics. Water Resour. Res. 57, e2021WR030248.

Payn, R.A., Gooseff, M.N., McGlynn, B.L., Bencala, K.E., Wondzell, S.M., 2009. Channel water balance and exchange with subsurface flow along a mountain headwater stream in Montana, United States. Water Resour. Res. 45, W11427.

Pinder, G.F., Sauer, S.P., 1971. Numerical simulation of flood wave modification due to bank storage effects. Water Resour. Res. 7 (1), 63–70.

Schmadel, N.M., Ward, A.S., Lowry, C.S., Malzone, J.M., 2016. Hyporheic exchange controlled by dynamic hydrologic boundary conditions: Dynamic hyporheic exchange. Geophys. Res. Lett. 43 (9), 4408–4417.

Shuai, P., Chen, X., Song, X., Hammond, G.E., Zachara, J., Royer, P., Ren, H., Perkins, W. A., Richmond, M.C., Huang, M., 2019. Dam operations and subsurface hydrogeology control dynamics of hydrologic exchange flows in a regulated river reach. Water Resour. Res. 55, 2593–2612. https://doi.org/10.1029/2018WR024193.

Storey, R.G., Howard, K.W., Williams, D.D., 2003. Factors controlling riffle-scale hyporheic exchange flows and their seasonal changes in a gaining stream: a three-dimensional groundwater flow model. Water Resour. Res. 39 (2), 1034. https://doi.org/10.1029/2002WR001367.

Tonina, D., Buffington, J.M., 2007. Hyporheic exchange in gravel bed rivers with pool-riffle morphology: Laboratory experiments and three-dimensional modeling. Water Resour. Res. 43, W01421. https://doi.org/10.1029/2005WR004328.

Trauth, N., Fleckenstein, J.H., 2017. Single discharge events increase reactive efficiency of the hyporheic zone. Water Resour. Res. 53 (1), 779–798.

Tunas, I.G., 2019. The application of ITS-2 model for flood hydrograph simulation in large-size rainforest watershed, Indonesia. J. Ecol. Eng. 20 (7), 112–125. https://doi.org/10.12911/22998993/109882.

Wang, L., Jiang, W., Song, J., Dou, X., Guo, H., Xu, S., Zhang, G., Wen, M., Long, Y., Li, Q. i., 2017. Investigating spatial variability of vertical water fluxes through the streambed in distinctive stream morphologies using temperature and head data. Hydrogeol. J. 25 (5), 1283–1299.

Ward, A.S., Gooseff, M.N., Voltz, T.J., Fitzgerald, M., Singha, K., Zarnetske, J.P., 2013. How does rapidly changing discharge during storm events affect transient storage and channel water balance in a headwater mountain stream? Water Resour. Res. 49 (9), 5473–5486.

Westhoff, M.C., Gooseff, M.N., Bogaard, T.A., Savenije, H.H.G., 2011. Quantifying hyporheic exchange at high spatial resolution using natural temperature variations along a first-order stream. Water Resour. Res. 47 (10), W10508.

Wondzell, S.M., 2006. Effect of morphology and discharge on hyporheic exchange flows in two small streams in the Cascade Mountains of Oregon. USA. Hydrol. Process. 20 (2), 267–287.

Wörman, A., Packman, A.I., Johansson, H., Jonsson, K., 2002. Effect of flow-induced exchange in hyporheic zones on longitudinal transport of solutes in streams and rivers. Water Resour. Res. 38(1) https://doi.org/0043-1397/02/2001WR00769.

Xue, Y., Xie, C., 2007. Numerical Simulation for Groundwater (in Chinese). Science Press, Beijing.

Yue, S., Ouarda, T.B.M.J., Bobée, B., 2001. A review of bivariate gamma distributions for hydrological application. J. Hydrol. 246 (1), 1–18.

Zeleke, T.B., Si, B.C., 2005. Scaling Relationships between Saturated Hydraulic Conductivity and Soil Physical Properties. Soil Sci. Soc. Am. J. 69 (6), 1691–1702.

Zhang, Y., Green, C.T., Baeumer, B., 2014. Linking aquifer spatial properties and non-Fickian transport in mobile–immobile like alluvial settings. J. Hydrol. 512 (9), 315–331.

Zhang, Y., Sun, H., Stowell, H.H., Zayernouri, M., Hansen, S.E., 2017. A review of applications of fractional calculus in Earth system dynamics. Chaos Soliton Fract. 102, 29–46.

Zimmer, M.A., Lautz, L.K., 2014. Temporal and spatial response of hyporheic zone geochemistry to a storm event. Hydrol. Process. 28 (4), 2324–2337.